

THESIS

STABLE AND UNSTABLE TILING PATTERNS OF ABC MIKTOARM TRIBLOCK
TERPOLYMERS STUDIED VIA GPU-ACCELERATED SELF-CONSISTENT FIELD
CALCULATIONS

Submitted by

Cody Hawthorne

School of Advanced Materials Discovery

In partial fulfillment of the requirements

For the Degree of Master of Science

Colorado State University

Fort Collins, Colorado

Summer 2022

Master's Committee:

Advisor: David (Qiang) Wang

Travis Bailey
Garrett M. Miyake
Grzegorz Szamel

Copyright by Cody M. Hawthorne 2022

All Rights Reserved

ABSTRACT

STABLE AND UNSTABLE TILING PATTERNS OF ABC MIKTOARM TRIBLOCK TERPOLYMERS STUDIED VIA GPU-ACCELERATED SELF-CONSISTENT FIELD CALCULATIONS

Block copolymers are macromolecules formed from linking together two or more chemically distinct types of polymers. Provided the different monomers that make up each polymer are immiscible enough, melts of these molecules will self-assemble into highly ordered, periodic structures at length scales typically on the order of nanometers. The exemplary and simplest material in this respect is the AB diblock copolymer, a linear macromolecule formed by bonding together two immiscible polymers (or ‘blocks’) A and B. This material is capable of assembling into lamellar, cylindrical, spherical, and networked morphologies depending on the length of the A block and degree of immiscibility between A and B. The ability to control bulk properties of block copolymers via tuning these molecular properties, as well as the length scales that these ordered structures form at, makes them intriguing candidates for next generation technological applications in lithography, photonics, and transport. In order to realize these applications it is imperative to have an intimate understanding of the phase behavior of the materials such that the morphology that will form at a given combination of parameters can be predicted reliably.

Self-consistent field theory, or SCFT, has emerged as a useful theory for investigating block copolymer phase behavior. This statistical-mechanical theory has been successfully used to construct phase diagrams of the self-assembled morphologies of various block copolymer systems.

These phase diagrams provide the connection between molecular properties (such as block lengths, block incompatibility, and chain architecture) and bulk properties necessary in order to control the behavior of the material. The theory must, in general, be solved numerically – an open-source software termed ‘PSCFPP’ has recently been made available for this purpose, capable of implementing high-performance SCFT calculations for arbitrarily complex acyclic block copolymers by taking advantage of the massive parallelization of GPUs.

In this work, PSCFPP is used to apply SCFT to a neat melt of complex ABC miktoarm triblock terpolymers, which are an interesting class of block copolymer formed by linking three distinct polymers A, B, and C at a single junction point. The resulting star-shaped macromolecule is referred to as a ‘miktoarm’ and exhibits unique morphologies such as the Archimedean tiling patterns that cannot be found in other block copolymer materials. To focus on the effect of composition, which has not yet been fully elucidated, we restrict the interaction parameters between monomers ABC to the symmetric case where all are equivalent. The central region of the phase diagram, where the effect of the miktoarm architecture is most significant, is mapped out in detail and a 3D morphology previously thought to be metastable is shown to be a stable phase. Further, discrepancies in the literature concerning the stability of multiple 2D tiling patterns are resolved such that the phase diagram presented is the most accurate for the system to date. Finally, a 2D morphology of some interest owing to the possibility of exhibiting photonic band gaps is definitively shown to be stable in this system and its thermodynamic properties analyzed to ascertain what drives its formation. These results provide a solid foundation for further refinement of our understanding of ABC miktoarm phase behavior and demonstrate the utility of a software such as PSCFPP for obtaining high-accuracy SCF results.

ACKNOWLEDGEMENTS

I would like to gratefully acknowledge the financial support provided by SAMD and the CSU Physics Department during the time I spent working on this project, as well as the guidance and assistance provided by Prof. Wang and Juntong He (a PhD student in Prof. Wang's group), the latter of whom implemented all of the numerical methods used by us in PSCFPP. Carolina Bañuelos (the SAMD Program Manager) and Prof. Travis Bailey (the SAMD Director) have also provided me with guidance during my time at CSU, and without Prof. Bailey's encouragement I may not have reached out to Prof. Wang about joining his group.

TABLE OF CONTENTS

ABSTRACT	ii
ACKNOWLEDGEMENTS	iv
Chapter 1 – Introduction	1
Chapter 2 – Theory and Methods	17
Theory	17
Methods	22
Chapter 3 – Results	30
Numerical Accuracy	30
Phase Diagram	35
Free Energy and Stability Analysis	39
Chapter 4 – Conclusions.....	48

Chapter 1: Introduction

Block copolymers (BCPs) are a fascinating class of materials formed from covalently bonding two or more chemically distinct (immiscible) polymers together. Owing to the thermodynamic incompatibility between the different polymers (referred to as ‘blocks’) the materials would ideally like to undergo macrophase separation – however, the covalent bonds limit the spatial segregation that can be achieved.¹ This results in the formation of so-called ‘microphases’ where the different blocks phase-separate into highly ordered, periodic structures at length scales on the order of a BCP’s radius of gyration, i.e., nanometers. Even in the simplest type of BCP system, consisting of two distinct homopolymers A and B bonded together and referred to as an AB diblock copolymer, there is a rich variety of microphases (or ‘morphologies’) that the BCPs can arrange themselves in. While interesting from a fundamental perspective owing to the physics that govern this phenomenon and extraordinary patterns that can be formed, these materials also show great potential for next generation technological applications including nanostructured membranes and reactors, photonic crystals, and high-density information storage media.² In order to realize these applications, it is imperative to have precise control over both the morphology formed by a given BCP system and the properties of that morphology, such as bulk period and stability.

Self-consistent field theory, or SCFT, has proven to be a useful theory for studying the statistical thermodynamics of condensed polymer systems.³⁻⁵ It provides a connection between the properties of individual polymers and the bulk properties of a morphology, serving as a guide for how the former can be used to control the latter. It additionally provides an expression for the Helmholtz free energy that can be evaluated for any specified morphology, thus allowing the construction of phase diagrams by comparing the free energies of competing phases. Within SCFT

of the ‘standard’ model (i.e., incompressible melts of continuous Gaussian chains with Dirac δ -function interactions), the phase behavior of a system is described by binary Flory-Huggins interaction parameters $\chi_{\alpha\beta}$ between distinct species α and β as well as the degree of polymerization N , the block (volume) fraction of species P $f_P \equiv N_P/N$, and the statistical segment lengths b_P . The block fraction of a component is simply the fraction of the total BCP’s length occupied by that species (with all monomers occupying the same volume), while only the products of the Flory-Huggins parameters and N are accessible quantities – strictly speaking, N is infinite and $\chi_{\alpha\beta}$ infinitesimal within the theory. For example, in a neat melt of conformationally symmetric AB diblock copolymers the phase behavior is governed by two parameters: $\chi_{AB}N \equiv \chi N$ and $f_A \equiv f$. Here, conformationally symmetric means that the statistical segment lengths of both blocks are equal. As the number of components increases and polymer topology becomes more complex, both parameter space and morphology space inflate drastically – introducing one more component to create an ABC triblock terpolymer results in phase behavior that is governed by five parameters, $\chi_{AB}N$, $\chi_{BC}N$, $\chi_{AC}N$, f_A , and f_B , with dozens of ordered phases having been found to exist.⁶ The topology of the polymer has an effect as well, for an ABC triblock can be synthesized to be either linear or branched – further, for linear ABC triblocks even the sequencing of the blocks has been shown to have an influence on the phase behavior.⁶

The mathematical form of SCFT is that of a classical field theory that reduces the many-body problem of polymers in a melt interacting with each other to the problem of a single chain interacting with an external potential field created by the other chains in the system. The fundamentals were elaborated by S. F. Edwards during the 1960s while the theory was first applied to microphase separation in diblock melts by Helfand, Leibler, Semenov, and others during the 1970s-80s.⁷⁻⁹ These early attempts at solving the governing equations were forced to use additional

approximations in order to obtain the phase diagrams – the first accurate numerical solution of the SCF equations was obtained by Matsen and Schick in their seminal 1994 work where they utilized the spectral method to compute the phase diagram for a neat melt of diblock copolymers.³ Since then there has been a flurry of activity centered around BCPs, both theoretically and experimentally – SCFT in particular has been used by a large number of groups around the world to investigate the morphological behavior of a wide range of BCP systems. However, while our understanding of the AB diblock copolymer is reaching a state of great maturity the same cannot be said for more sophisticated types of polymer materials. This is largely a symptom of the complexity that comes packaged with these materials, as discussed for the case of ABC triblocks vs AB diblocks. In order to elucidate the large number of morphologies available to these complex BCPs and attain a thorough understanding of their phase behavior it is necessary to utilize a combined theoretical and experimental approach. In this work, a contribution is made to the former: SCFT will be used to study the morphological behavior of a class of BCPs referred to as ABC miktoarm, or star, terpolymers. These molecules, a schematic of which is shown in Fig. 1.1b, are the branched counterparts to linear ABC triblocks. This unique topology enforces a strong

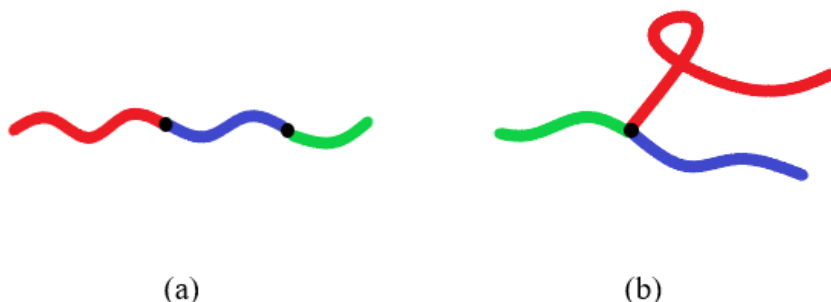


Figure 1.1 Linear (a) vs miktoarm (b) topologies for ABC triblock terpolymers with $f_A > f_B > f_C$.

constraint on the morphologies that can be formed, causing the phase behavior to deviate significantly from their linear counterparts and resulting in a number of fascinating morphologies that have not been observed in other BCP systems.

Before the results of this work are described it is appropriate to summarize the current state of our theoretical understanding of the morphological behavior of ABC miktoarm terpolymers. To make the following discussion more comprehensible, a collection of prominent morphologies formed by neat melts of these molecules is shown in Fig. 1.2 at $\chi N \equiv \chi_{AB}N = \chi_{BC}N = \chi_{AC}N = 30$ and various block fractions. The unit cell used in computations is given as the area enclosed by the lines emanating straight from each tick on the sides of the plots, with the qualitative magnitude of any cell parameter indicated by the distance between its ticks. For all 2D phases, these plots are generated from the converged volume fraction fields $\phi_P(\mathbf{r})$ for species P at a set of block fractions $\{f_P\}$ where that morphology is stable. Regions where $\phi_P(\mathbf{r}) > 0.5$ are denoted by red, blue, and green for species A, B, and C, respectively, and the plots are created by overlaying the volume fraction fields for each species. To do this, each species is given a custom colormap that is transparent when $\phi_P(\mathbf{r}) < 0.5$ and transitions from white at $\phi_P(\mathbf{r}) = 0.5$ to a deep red, blue, or green at $\phi_P(\mathbf{r}) = 1$. In this way, the intensity of the color corresponds to the concentration of the respective species – however, note that this visualization method destroys some information about the transition from $\phi_P(\mathbf{r}) = 0.5$ to $\phi_P(\mathbf{r}) \approx 0$ as this region is set to be transparent for all species. Nevertheless, it provides a more detailed picture of the morphology than most other visualizations in the literature where binary colormaps are used that are transparent for $\phi_P(\mathbf{r}) < 0.5$ and a solid red, blue, or green for $\phi_P(\mathbf{r}) \geq 0.5$. The 1D plot is straightforward with red, blue, and green denoting the volume fraction curves for species A, B, and C, respectively, while the 3D plots (from Ref. 12) are colored according to the binary colormaps described above.

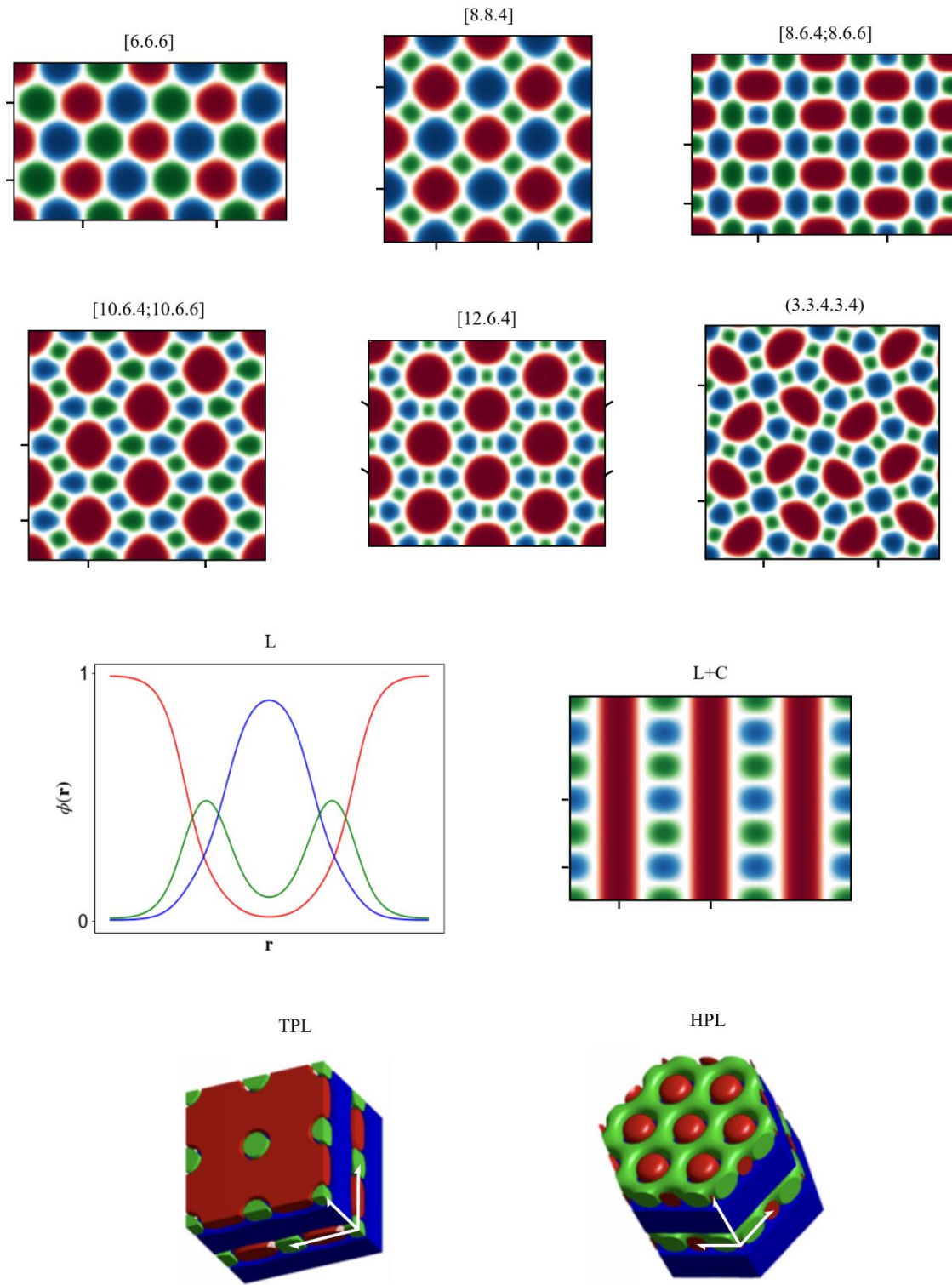


Figure 1.2 Prominent morphologies formed by ABC miktoarm terpolymers near the center of the phase diagram at $\chi N = 30$. The 3D plots of TPL and HPL are pulled from Ref. 12 while all others are generated in-house. Basis vectors of the unit cell considered in computations are shown in white for the 3D morphologies.

The names given to each morphology are shown above the corresponding plots – for the 2D tiling patterns, the naming convention is generally well-accepted and straightforward. Each tiling pattern is described by a set of vertices based on the number and type of polygons that meet at a given vertex; each polygon is denoted by the number of sides it has (or equivalently the number of nearest-neighbor polygons) while unique polygons are separated by periods – for example, in the [6.6.6] tiling pattern every vertex can be described as the junction point of three hexagons. In the [12.6.4] pattern the majority domains (in red) are surrounded by twelve polygons, the blue domains by six polygons, and the green domains by four polygons. If the pattern contains more than one unique vertex, then these are separated by semicolons as in the [8.6.4;8.6.6] and [10.6.4;10.6.6] morphologies. The (3.3.4.3.4) phase is a notable exception to this rule – if the above convention were used then it would be denoted by [10.6.4;10.8.4]. However, Matsushita and co-workers noticed¹⁰ that the (3.3.4.3.4) Archimedean tiling pattern can be overlaid on this morphology with the vertices centered on the larger red domains in Fig. 1.2. This convention has generally been accepted by the community¹¹⁻¹³ and so we adopt it here for consistency – note that parentheses are used rather than brackets to denote that the tiling pattern is an overlaid rather than direct one.

All of the tiling patterns are 2D cylindrical structures with the cross-sections of the cylinders taking on various distinct geometries – they are also all stable near the center of the phase diagram. Once one progresses radially outward more, the dominant phases transition from the tiling patterns to various forms of lamellae, shown as the bottom four phases in Fig. 1.2. The 1D morphology denoted by L is a variation of the simple lamellae observed in linear ABC triblocks or AB diblocks. The smallest C arm segregates from the A and B arms as much as it can while the topological constraint of the miktoarm junction prevents total segregation from being possible. As

such, the C arm is constantly in contact with A and B arms leading to a unique three-phase lamellar structure. This plot of L is shown for $f_A = 0.5$, $f_B = 0.3$ – it needs to be noted, however, that as the length of the A block is increased and the B block decreased (while holding C constant) the morphology will transition to one where the B and C blocks no longer separate and instead occupy disordered lamellar regions between the A domains. Here we make no attempt to differentiate between the two as it is found in our calculations that the three-phase structure will spontaneously convert to the two-phase structure as f_A is increased. This phenomenon is discussed in more detail for the tiling patterns in Chap. 3.3 .

The 2D morphology labelled L+C (Lamellae + Cylinders) is a well-known one in ABC miktoarms¹³ and has been referred to with various names in other studies – here we use the simplest one that captures the essence of the phase. Finally, the two 3D morphologies considered in this study are shown at the bottom of Fig. 1.2 and denoted by TPL (Tetragonally Perforated Lamellae) and HPL (Hexagonally Perforated Lamellae) with the plots being reproduced from Ref. 12. The two morphologies are identical with the exception of the packing arrangement of the cylindrical structures, which is tetragonal in TPL and hexagonal in HPL as their names would suggest. Note that the colors of these 3D plots are not consistent with the others, though they are sufficient to convey the structure of the morphology: the largest block occupies a lamellar region while the two smaller blocks occupy a perforated lamellar region with the smallest block forming the perforations and the middle block the matrix around them.

To gauge the current state of the art in SCF studies of ABC miktoarms a comprehensive survey of the literature was conducted – owing to the relatively recent introduction of the numerical methods requisite for solving SCFT^{3, 8, 14} and the (until very recently¹⁵) lack of open-source software for implementing said methods there has been a limited amount of progress made in this

area. Here we summarize the past studies done on this material using SCFT, focusing on the case of symmetrically interacting ABC miktoarms and including studies where a thorough attempt at mapping out a phase diagram was made. To better facilitate comparison with the results presented in this work, as much information as was made available in the relevant publications is included such as numerical methods, numerical parameters, candidate phases, and phases found to be stable. However, it has been noted⁵ that many SCF studies do not provide information at a level that can be used to replicate their results. We also find this to be the case and attempt to remedy it by including detailed information in the results section – additionally, the use of a freely available open-source software in this work will make the process of replicating our results trivial.

Note that in all SCFT studies of ABC miktoarms only the conformationally symmetric molecules are considered where all statistical segment lengths are equal. A first attempt at mapping out the phase diagram of ABC miktoarms with SCFT was made in 2004¹⁶ where the real-space method of Drolet and Fredrickson⁸ (i.e., the Crank-Nicolson with alternating-direct implicit method) was used to solve the SCF equations. Note that this scheme uses a linear mixing of old and new solutions as the field update algorithm, while the error ε was chosen to be gauged by the relative change in the dimensionless Helmholtz free energy per chain βf_c at each iteration with $\beta \equiv 1/k_B T$. Iteration was continued until $\varepsilon < 10^{-4}$, and βf_c was minimized with respect to the cell parameters with a rectangular calculation cell used for all morphologies. A contour discretization of $N_s = 100$ was used although it is unclear what the spatial discretization was, which has a significant effect on the accuracy of βf_c as will be discussed in Chap. 3.1. Two combinations of segregation strengths were considered, the symmetric case with $\chi N \equiv \chi_{AB}N = \chi_{BC}N = \chi_{AC}N = 35$ and the asymmetric case with $\chi_{AB}N = \chi_{BC}N = 72$, $\chi_{AC}N = 22$. Only 1D/2D phases were considered, and for the symmetric case the stable phases are given as core-

shell hexagonal cylinders (H), lamellae (L), the knitting pattern (K), lamellae combined with cylinders (L+C), lamellae with beads at the interface, and the [6.6.6], [8.8.4], and [10.6.4;10.6.6] tiling patterns. Notably, many significant phases are not included in their computations such as [12.6.4], [8.6.4;8.6.6], and (3.3.4.3.4). Although the entire region of the phase diagram was considered (rather than just the central part), the diagrams presented are quite coarse, giving the stable phases at block fraction increments of 0.1 – owing to the limited number of candidate phases considered and coarseness of the phase diagrams they are not reproduced here.

Two SCFT studies of ABC miktoarms appeared in 2010 – the first¹⁷ used a generic reciprocal-space method to solve the SCF equations, distinct from the spectral method of Matsen and Schick³ as it does not use symmetry adapted basis functions. A relaxation method was used as a field update algorithm while the error was measured by the relative change in f_c – iteration progressed until $\varepsilon < 10^{-6}$. The free energy was minimized with respect to cell parameters, and in all reciprocal-space calculations they used 151 basis functions (corresponding to a spatial discretization of $\sim 12^2$) – to justify this choice they compared their results for f_c to results from the spectral method and found them to agree to within 0.2% for $\chi N = 30$ where all calculations were done. Only 1D/2D phases were considered, and for $\chi N = 30$ the stable phases are given as L, L+C, and the [6.6.6], [8.6.4;8.6.6], [10.6.4;10.6.6], [12.6.4], and [8.6.4;8.8.4;12.6.4;12.8.4] tiling patterns – this last phase has not been observed in any other theoretical or experimental studies. Notably, the (3.3.4.3.4) morphology was not considered. The phase diagram is presented in Fig. 1.3a with block fraction increments of 0.001, as well as the stable phases along the $f_A = f_B$ isopleth in 1.3b. In the phase diagram, 6 denotes the [8.6.4;8.8.4;12.6.4;12.8.4] tiling pattern found to be stable while there is a mistake in the name of [10.6.4;10.6.6] in the article with an extra vertex being included.

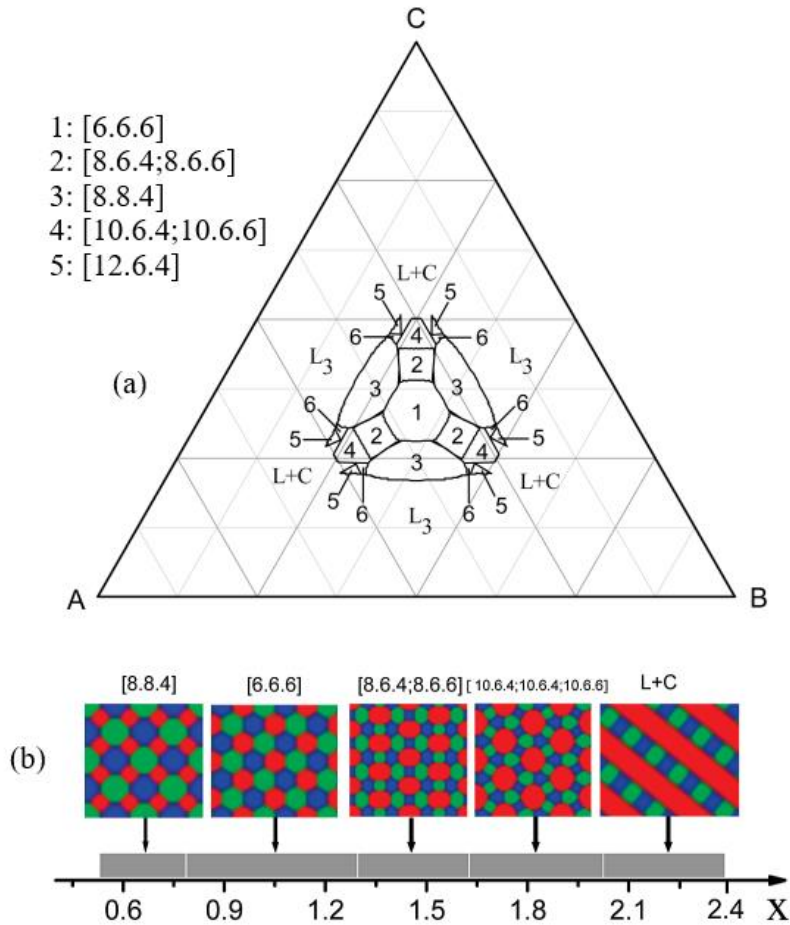


Figure 1.3 Phase diagram (a) and stable phases along $f_A = f_B$ isopleth (b) at $\chi N = 30$, reproduced from Ref. 17. Here $X = f_C/f_A$ and the [12.6.4] pattern is notably not found to be stable along the isopleth.

The second SCFT study of ABC miktoarms in 2010¹⁸ was by the same research group and expanded upon the work done previously. The methods differ in that the generic reciprocal-space method is used first as a screening technique to locate potential phases that are then fed to a real-space method based on the second-order pseudospectral algorithm.¹⁴ The field update algorithm and measure of error were not given, although a contour discretization of $N_s = 1000$ was used and tested to support that it yielded an accuracy of 10^{-3} in f_c . Mesh sizes of 128^2 and 64^3 were used in 2D and 3D calculations, respectively, and it is stated that these were enough to yield 10^{-8}

accuracy in βf_c . Calculations were done at $\chi N = 60$ and considered 1D/2D phases, including (3.3.4.3.4) and a new [8.6.4;8.6.6;12.6.4] tiling pattern, as well as a single 3D phase that had not been considered theoretically before known as HHC (Hexagonal Hierarchical Cylinders). HHC consists of small cylindrical domains formed by alternating minority blocks stacked vertically and surrounded by a matrix of the largest block. Stable phases and the phase diagram are given in Fig. 1.4a, while βf_c -data and phase boundaries along the $f_B = f_C$ isopleth are shown in Figs. 1.4b and 1.4c. Note that L3 is equivalent to L while HC corresponds to the standard core-shell hexagonal cylinder morphology known from linear triblocks.

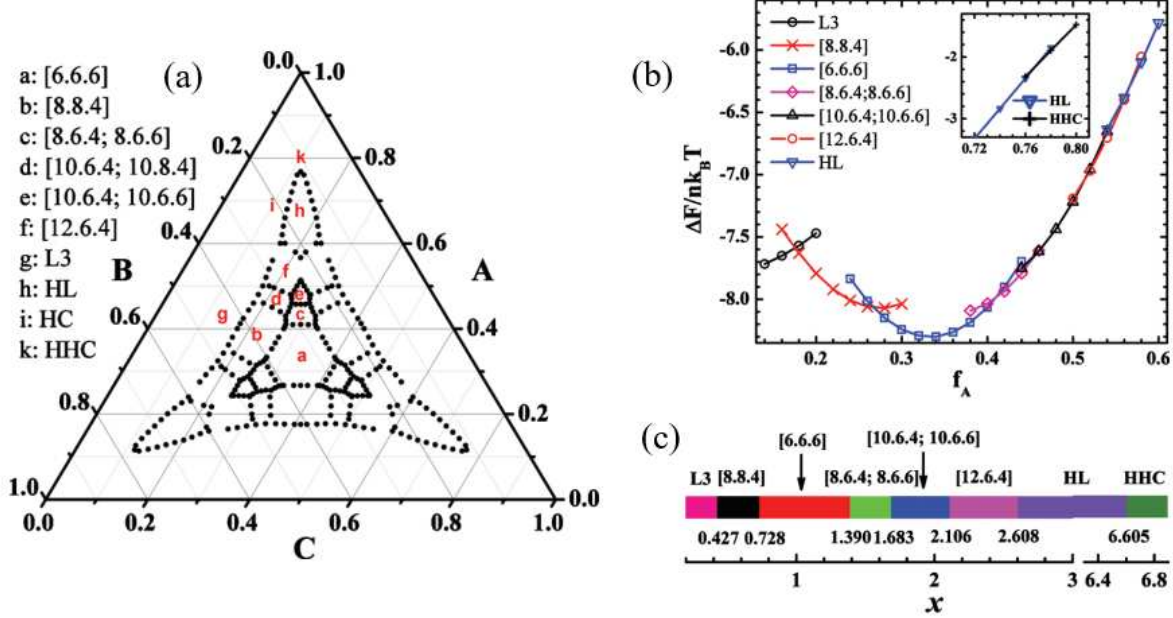


Figure 1.4 Phase diagram (a) and data along the $f_B = f_C$ isopleth (b) and (c) at $\chi N = 60$, reproduced from Ref. 18. Here $x = f_A/f_B$ and the (3.3.4.3.4) and L+C phases are referred to as [10.6.4;10.8.4] and HL, respectively, while HC and HHC denote morphologies found near the outer regions of the phase triangle.

Finally, the phase behavior of symmetrically interacting ABC miktoarms was tackled with SCFT in a study published in 2013¹² that notably extended the computations to consider a large number of 3D phases. The fourth-order pseudospectral algorithm¹⁹ was used with all spatially

varying functions being expanded in plane waves with 32^3 basis functions, corresponding to a spatial discretization of 32^3 . The contour discretizations used were varied and not stated explicitly, although it was required in all computations that $N_s \geq 100$. A large number of candidate phases are presented, many of them 3D in nature – additionally it is stated that all previously discovered 1D/2D phases were considered. Calculations were done at $\chi N = 30$ along five lines connecting the center of the phase triangle to five points where the typical diblock phases are stable, and the stable phases as well as the phase diagram are shown in Fig. 1.5 – notably, only one 3D phase (TPL) is found to be stable near the center of the phase diagram.

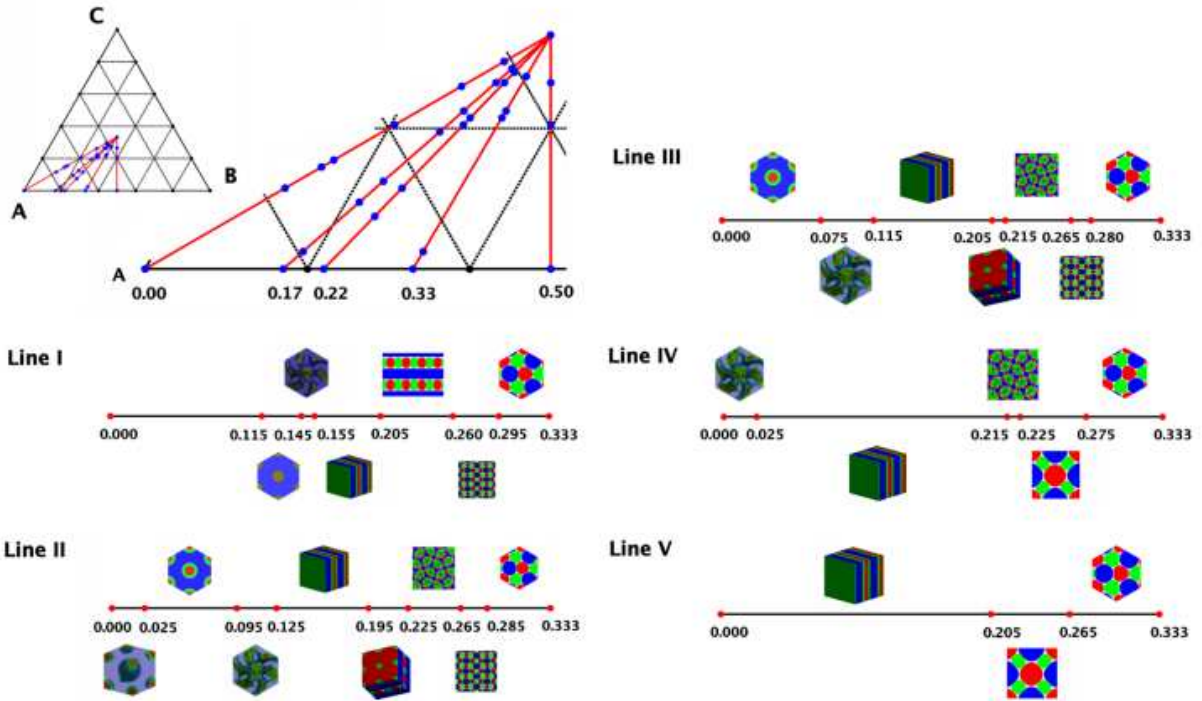


Figure 1.5 Phase diagram for $\chi N = 30$ reproduced from Ref. 12. The values along the bottom of the triangle denote f_B while those along lines I-V denote f_C , and the lines go in ascending order from left to right. Note that the [12.6.4] and [10.6.4;10.6.6] patterns do not appear anywhere in this diagram despite it being the most recent application of SCFT to symmetrically interacting ABC miktoarms.

On the experimental side, a significant amount of work on the phase behavior of ABC miktoarm terpolymers has been carried out by Matsushita and co-workers.^{10, 13, 20, 21} Generally, the systems studied consisted of two types of blends, the first being polystyrene-polyisoprene-poly(2-vinylpyridine) (PS-PI-P2VP) miktoarms with PI or PS homopolymers and the second two types of PS-PI-P2VP miktoarms with variable block fractions of one component. It has been argued¹⁰ that blending miktoarms with low molecular weight homopolymers of one of the arms causes little difference in the resulting morphology from that of neat miktoarms while allowing easy control of composition. The addition of homopolymer could, however, shift the locations of phase boundaries at a given degree of segregation. Even if experiments were done on neat melts of PS-PI-P2VP miktoarms rather than blends, there would still be a number of discrepancies between the model system of symmetrically interacting neat melts considered in this (and previous^{12, 16-18}) work and the systems studied by experimentalists. Most significantly, the interactions in PS-PI-P2VP are known to be asymmetric and obey $\chi_{IS} \approx \chi_{SP} < \chi_{IP}$, which drastically affects phase behavior.^{10, 17, 22} Additionally, effects ignored in SCFT of the standard model such as fluctuations, polydispersity, finite chain length, conformational asymmetry, impurities, and slow kinetics can all impact the experimentally observed morphologies. Nevertheless, experimental observations serve as an invaluable guide for studying unfamiliar BCP systems with SCFT. We note that the morphologies proven to be stable in this work have all been observed experimentally, including a 3D phase previously found to be metastable for a symmetrically interacting system.¹² For the previous reasons, no attempt is made to quantitatively compare SCFT and experimental results – however, TEM images of the experimentally observed counterparts to most of the morphologies given in Fig. 1.2 are provided in Fig. 1.6 for qualitative comparison.

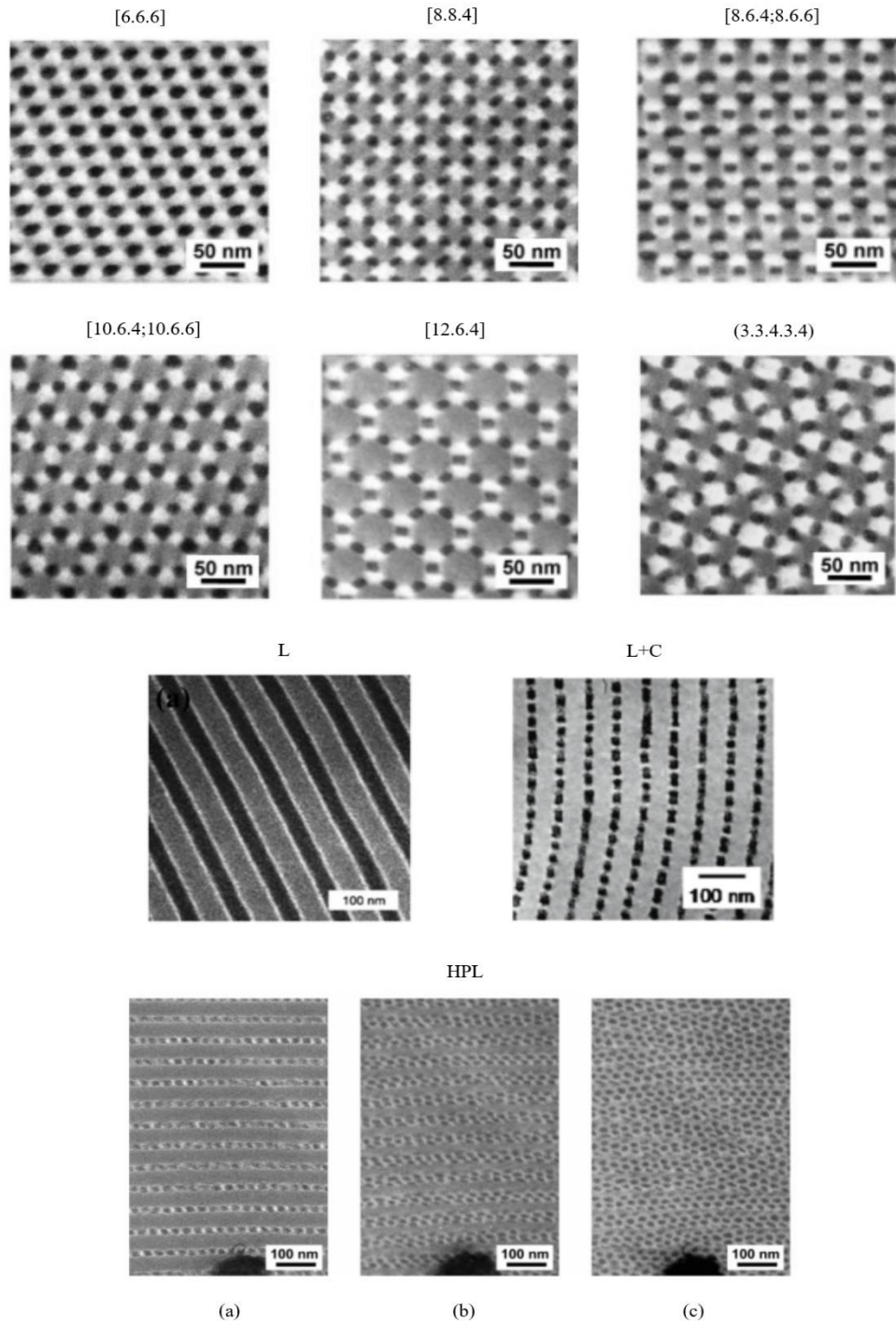


Figure 1.6 TEM images of all morphologies shown in Fig. 1.2 except TPL for various block fractions and segregation strengths, reproduced from Refs. 10, 13, 19, and 20. Morphologies shown were obtained from a system of PS-PI-P2VP except for L, which was obtained from PS-PB-P2VP (PB=poly(1,2-butadiene)). The images for HPL show the morphology at tilt angles of 0° (a), 25° (b), and 35° (c) about a horizontal axis.

In this thesis, the SCF equations for a neat melt of symmetrically interacting ABC miktoarm terpolymers are solved numerically using a modified version of ‘PSCFPP’ (Polymer Self Consistent Field Plus Plus). This open-source software, developed by David Morse and coworkers, has been recently described in the literature¹⁵ and is an evolution of the older ‘PSCF’ software from the same group.⁵ PSCFPP allows SCF calculations to be done for melts of arbitrarily complex acyclic BCPs, utilizing GPU-accelerated code to significantly speed up the computations. Here it is used to compute, at high accuracy, the central region of the ternary phase diagram at $\chi N = 30$ by comparing the Helmholtz free energy per chain of various candidate morphologies. Ten possible ordered phases are considered, all shown in Fig. 1.2 – as there are an enormous number of possible phases with the vast majority being metastable, candidate morphologies were selected based on previous theoretical^{12, 16-18} and experimental^{10, 20, 21} studies.

Notably, the previous theoretical studies using SCFT have a number of discrepancies – Refs. 12, 17, and 18 compute the phase diagrams for symmetrically interacting ABC miktoarms at $\chi N = 30$, 30, and 60, respectively. As the same theory is being solved at the same parameter values, the results from Refs. 12 and 17 should agree exactly provided that the same candidate phases were considered, the free energy accuracy was carefully examined, and the optimal cell parameters were found. However, Ref. 17 does not find (3.3.4.3.4) to be stable but does find [12.6.4] and [10.6.4;10.6.6] to be stable while Ref. 12 does not have either of these as stable but does have (3.3.4.3.4) and TPL. The reason (3.3.4.3.4) and TPL do not show up in Ref. 17 is simply because they were not considered as candidate phases – that both studies considered [12.6.4] and [10.6.4;10.6.6], however, leads us to question which is correct. The phase diagram presented for $\chi N = 60$ in Ref. 18 contains significantly shifted phase boundaries from the others, yet also has [12.6.4], [10.6.4;10.6.6], and (3.3.4.3.4) all showing regions of stability. This raises the question

of whether these phases enter into the diagram at larger degrees of segregation or if they can be found at smaller χN , which has profound consequences for our understanding of ABC miktoarm phase behavior.

This work will resolve these discrepancies and present a refined phase diagram for $\chi N = 30$, mapping out the central region in detail. An accuracy study will be presented to assure the quality of the results, as well as free energy data along the $f_B = f_C$ isopleth to justify the stable phases and compare with other work. Further, a case study of the stability of (3.3.4.3.4) will be presented with the various energetic and entropic contributions to the Helmholtz free energy per chain decomposed into their constituents for all phases and compared. First, the theory will be presented in Chap. 2.1 – the self-consistent field theory of neat BCP melts has become well-developed by this point and the reader interested in further details should consult any of the excellent references that exist.^{3, 4, 7, 9, 23} The methods used to solve the theory and generate trial fields will be discussed next in Chap. 2.2, followed by a presentation and analysis of the results in Chap. 3. Finally, in Chap. 4 the successes and shortcomings of the present study will be addressed and an outlook for future work on ABC miktoarms will be provided.

Chapter 2: Theory and Methods

I. Theory

Here the fundamentals of the polymer self-consistent field (SCF) theory are discussed and the SCF equations for the system of interest (i.e., neat melts of ABC miktoarm terpolymers) presented, along with some related thermodynamic quantities obtained from decomposing the Helmholtz free energy. The SCF theory is described in detail elsewhere^{4, 17} and is a straightforward generalization of the classic theory developed for diblock copolymers.

SCF theory is a statistical field theory that is usually based on the ‘standard’ model, where a polymer chain is described as a continuous curve in space, much like that shown in Fig. 1.1. The local, atomic details of the polymer are abstracted away, and a coarse-grained perspective is taken on its structure by allowing the degree of polymerization N to approach infinity and the monomer size (thus the range of their short-range interactions) to approach zero. This model allows the statistical mechanics of the polymer to be reduced to solving a partial differential equation rather than evaluating a large number of integrals, as would be the case for a model that treats the polymer as having finite N (and interaction range). Specifically, the polymers are treated as an incompressible melt of continuous Gaussian chains under the influence of external potential fields. Interactions between the monomers are taken into account via the Dirac δ -function interactions such that the Hamiltonian for the system contains terms related to the conformational entropy of the molecules and the interaction energy of the system.

The many-chain canonical partition function is first written down for the particle-based system of an incompressible melt of continuous Gaussian chains – as the chains are continuous, their statistical mechanics is governed by path integrals over all possible conformations. Standard

field-theoretic transformations are then used to convert the particle-based system to a field-based one, where the distribution of a species in space is described by a continuous scalar function (i.e., the chain propagator). The many-chain partition function then takes the form of a set of functional integrals over fluctuating fields – as there is no general method for evaluating these integrals, an approximation must be made. Long-chain polymer melts are a system well-suited to the mean-field approximation owing to the massive sizes of the molecules (and thus the many chains that a single chain interacts with), which has the effect of damping the fluctuations away from the ensemble average that are ignored at the mean-field level. This approximation evaluates the functional integrals at the extrema of the integrand, yielding a Helmholtz free energy functional and a set of equations governing its extrema (known as the self-consistent field equations). That the global minimum (the equilibrium morphology) satisfies these equations is a necessary but not sufficient condition for finding it – as many solutions as can be collected must be compared to determine the optimal one.

The system under consideration in this work is an incompressible melt of n symmetrically interacting ABC miktoarm terpolymers in a unit cell of volume V subject to periodic boundary conditions. All length scales are expressed in units of the root-mean-square end-to-end distance of an ideal chain $R = b\sqrt{N}$ for statistical segment length b (assumed to be the same for all blocks P) and degree of polymerization $N = \sum_P N_P$. As usual, the block fraction of each species is denoted by $f_P = N_P/N$ such that $\sum_P f_P = 1$. Given a chemical potential field $\omega_P(\mathbf{r})$ for each species $P \in \{A, B, C\}$ the one-end integrated propagators $q_P(\mathbf{r}, s)$ and $q_P^\dagger(\mathbf{r}, s)$ are obtained via the modified diffusion equations

$$\frac{\partial q_P}{\partial s} = \frac{1}{6} \nabla^2 q_P - \omega_P(\mathbf{r}) q_P, \quad q_P(\mathbf{r}, 0) = 1 \quad (1)$$

$$-\frac{\partial q_P^\dagger}{\partial s} = \frac{1}{6} \nabla^2 q_P^\dagger - \omega_P(\mathbf{r}) q_P^\dagger, \quad q_P^\dagger(\mathbf{r}, f_P) = \prod_{P' \neq P} q_{P'}(\mathbf{r}, f_{P'}). \quad (2)$$

Here $s \in [0, f_P]$ corresponds to the scaled contour length along each arm of the polymer with $s = 0$ being the free end of any arm and $s = f_P$ the junction between the arms; the initial condition for Eq. (2) reflects the miktoarm topology of the polymer. The propagators $q_P(\mathbf{r}, s)$ and $q_P^\dagger(\mathbf{r}, s)$ are referred to as the forwards and backwards propagators, respectively – a successful solution of Eqs. (1) and (2) for these functions amounts to solving the statistical mechanics of a miktoarm subjected to the external fields $\{\omega_P(\mathbf{r})\}$. Once the propagators have been found, the normalized single-chain partition function Q can be computed as

$$Q = \frac{1}{V} \int d\mathbf{r} q_P(\mathbf{r}, s) q_P^\dagger(\mathbf{r}, s). \quad (3)$$

Note that this equality is independent of the value of s . Invoking the mean-field approximation to evaluate the many-chain partition function leads to the self-consistent field equations (4)-(6) and the dimensionless Helmholtz free energy per chain (7):

$$\phi_P(\mathbf{r}) = \frac{1}{Q} \int_0^{f_P} ds q_P(\mathbf{r}, s) q_P^\dagger(\mathbf{r}, s) \quad (4)$$

$$\omega_P(\mathbf{r}) = \chi N \sum_{P' \neq P} \phi_{P'}(\mathbf{r}) + \eta(\mathbf{r}) \quad (5)$$

$$\sum_P \phi_P(\mathbf{r}) = 1 \quad (6)$$

$$\beta f_c = -\ln Q + \frac{\chi N}{2V} \int d\mathbf{r} \left\{ \sum_P \sum_{P' \neq P} \phi_P(\mathbf{r}) \phi_{P'}(\mathbf{r}) \right\} - \frac{1}{V} \int d\mathbf{r} \left\{ \sum_P \omega_P(\mathbf{r}) \phi_P(\mathbf{r}) \right\}. \quad (7)$$

In Eq. (5), $\eta(\mathbf{r})$ is a Lagrange multiplier field that enforces the incompressibility condition Eq. (6) at every point in space. βf_c is a functional of the fields $\{\phi_{\mathbf{P}}(\mathbf{r})\}$ and $\{\omega_{\mathbf{P}}(\mathbf{r})\}$ – as each unique morphology has a unique set of these fields, each morphology has a unique value for βf_c . A phase diagram for the system can then be constructed by computing Eq. (7) for a set of candidate morphologies at a set of points in parameter space – the equilibrium morphology at any point in this space is that which minimizes βf_c . Additionally, the cell parameters of the unit cell affect βf_c as they constitute the upper bounds on all spatial integrals – any computation of Eq. (7) must thus also minimize it with respect to all cell parameters in order to find the bulk periodicity of an ordered phase. For a unit cell described by a set of parameters $\{\theta_i\}$, constituting all lengths and angles necessary to describe the geometry, the minimization of the free energy can be expressed as a requirement that¹⁵

$$0 = -\frac{1}{Q} \frac{\partial Q}{\partial \theta_i} \quad (8)$$

for all θ_i .

With an expression for the free energy in hand, the stability of different phases can be analyzed by decomposing Eq. (7) into its energetic and entropic contributions. For internal energy per chain u_c and entropy per chain s_c this yields

$$\beta u_c = \frac{\chi N}{2V} \int d\mathbf{r} \left\{ \sum_{\mathbf{P}} \sum_{\mathbf{P}' \neq \mathbf{P}} \phi_{\mathbf{P}}(\mathbf{r}) \phi_{\mathbf{P}'}(\mathbf{r}) \right\} \quad (9)$$

$$\frac{s_c}{k_B} = \ln Q + \frac{1}{V} \int d\mathbf{r} \left\{ \sum_{\mathbf{P}} \omega_{\mathbf{P}}(\mathbf{r}) \phi_{\mathbf{P}}(\mathbf{r}) \right\} \quad (10)$$

such that the free energy is recovered via $\beta f_c = \beta u_c - s_c/k_B$. The internal energy arises from unfavorable monomer-monomer contacts at the interfaces in the system while the entropy contains two contributions, the conformational entropy of the blocks and the translational entropy of the miktoarm junctions – the translational entropy of the blocks is included in the latter. The distribution of the junctions in space can also be studied by considering a junction density

$$\rho_J(\mathbf{r}) \equiv \frac{1}{Q} \prod_P q_P(\mathbf{r}, f_P) \quad (11)$$

such that $\int d\mathbf{r} \rho_J(\mathbf{r})/V = 1$. In this way, the quantity $\rho_J(\mathbf{r})d\mathbf{r} \equiv \rho_J(x, y, z)dx dy dz$ is interpreted as proportional to the probability that a miktoarm junction is located in a volume $d\mathbf{r}$ in the system. Equations (9) and (10) can then be decomposed further as

$$\beta u_c = \frac{1}{2} \sum_P \sum_{P' \neq P} \beta u_{c,PP'} \quad (12)$$

$$\frac{s_c}{k_B} = \sum_P \frac{s_{c,P}}{k_B} + \frac{s_{c,J}}{k_B} \quad (13)$$

with

$$\beta u_{c,PP'} \equiv \frac{\chi N}{V} \int d\mathbf{r} \phi_P(\mathbf{r}) \phi_{P'}(\mathbf{r}) \quad (14)$$

$$\frac{s_{c,P}}{k_B} \equiv \frac{1}{V} \int d\mathbf{r} [\omega_P(\mathbf{r}) \phi_P(\mathbf{r}) + \rho_J(\mathbf{r}) \ln q_P(\mathbf{r}, f_P)] \quad (15)$$

$$\frac{s_{c,J}}{k_B} \equiv -\frac{1}{V} \int d\mathbf{r} \rho_J(\mathbf{r}) \ln \rho_J(\mathbf{r}). \quad (16)$$

Equation (14) corresponds to the dimensionless internal energy per chain from the P-P' interactions while Eqs. (15) and (16) describe the dimensionless conformational entropy per chain

of the P-blocks and the dimensionless translational entropy per chain of the junctions, respectively; note that Eq. (16) is merely a functional analogue of the ideal entropy of mixing expression for component i $\Delta S_i^{\text{mix}}/nR = -x_i \ln x_i$.

II. Methods

To understand how solution of the SCF equations proceeds, note that from Eq. (5), for any species P the chemical potential $\omega_P(\mathbf{r})$ depends on the volume fractions of the other species $\phi_{P'}(\mathbf{r})$, which in turn depend on the propagators for those species via Eq. (4). But from Eqs. (1) and (2) the propagators for the other species in the system will also depend on $\omega_P(\mathbf{r})$ – the SCF equations thus form a non-linear set of equations that must be solved iteratively. Solution begins with trial fields for each of the $\omega_P(\mathbf{r})$ – the modified diffusion equations are then solved for the propagators, the single-chain partition function is evaluated, and the volume fractions $\phi_P(\mathbf{r})$ computed. The chemical potentials can then be recomputed via Eq. (5) from $\phi_P(\mathbf{r})$ – if the trial fields of $\omega_P(\mathbf{r})$ correspond to a solution, there will be no change in the fields from this process such that they have been determined self-consistently.

In general, however, the trial fields used will not correspond to a solution such that going through the steps will result in recomputed fields of $\omega_P(\mathbf{r})$ that are not consistent with the originally specified ones. The straightforward approach is to simply start the process over again with the recomputed $\omega_P(\mathbf{r})$, solve the MDEs again, and progress until a self-consistent solution is reached. In practice, though, this approach has rather poor numerical behavior and is unlikely to converge on a solution for most trial fields.¹⁴ It is thus necessary to use some form of field update algorithm (i.e., that for iteratively solving a set of non-linear equations) to both accelerate the iteration and improve its robustness such that the trial fields used do not need to be exceedingly close to a solution. With an update algorithm in hand, solution proceeds as described and iteration

is then progressed until some convergence criterion is met, which differs depending on the investigators. Once convergence is achieved, the free energy is computed via Eq. (7) and the process repeated for every morphology of interest. Aside from some minor differences arising from the subtleties of the theory, every implementation of SCFT will follow this basic solution process – it is in the specific choice of algorithms for solving the MDEs, evaluating integrals, and updating the chemical potential fields where implementations differ. The numerical methods used by PSCFPP are described at length in Refs. 4 and 15, although some are modified in the version used by the Wang group. Here we present a brief discussion of the numerical methods used and the parameters they introduce, focusing on those which affect the free energy accuracy most significantly.

The modified diffusion equations (MDEs) are solved using the pseudospectral (PS) method¹⁴ in tandem with Richardson extrapolation as introduced by Ranjan, Qin and Morse (RQM) with the fourth-order PS method¹⁹. The PS method discretizes the contour of the polymer into N_s steps with step-size $\Delta s = 1/N_s$. By accepting a global error of $O(\Delta s^2)$ the operators in the MDE are split, providing a formula that can be used to step along the chain contour from $s = 0$ to f_P and yield the propagators at each point along the chain:

$$q_P(\mathbf{r}, s + \Delta s) = \exp\left(-\frac{\omega_P(\mathbf{r})\Delta s}{2}\right) \exp(\Delta s \nabla^2) \exp\left(-\frac{\omega_P(\mathbf{r})\Delta s}{2}\right) q_P(\mathbf{r}, s) + O(\Delta s^3). \quad (17)$$

To evaluate this formula, two FFTs (Fast Fourier Transforms) are needed (or equivalently, one pair of FFT and iFFT) per contour step, which dominates the computational cost of the method. The RQM algorithm computes a PS solution with step-size Δs followed by another solution with step-size $\Delta s/2$, then uses Richardson extrapolation with this information to eliminate the leading-order term from the error series and yield an error of $O(\Delta s^4)$. This idea can be extended to

eliminate an arbitrary number of terms in the error series via successive step-size halving – to encapsulate all of these methods we refer to them as the REPS- K methods where K indicates the order of the method, or equivalently how many terms are removed from the error series. The pseudospectral method corresponds to REPS-0 and the RQM method to REPS-1 – note that while REPS-0 has a cost of two FFTs per contour step, REPS-1 has a cost of six. In general, the number of FFTs per contour step of the K^{th} REPS method is given by $2^{K+2} - 2$ while the size of the smallest step is $\Delta s/2^K$.

All integrals are computed using Romberg integration. The contour integrals in the expressions for $\phi_P(\mathbf{r})$ are computed such that the order of the integration method is matched to that of the REPS- K method used. The various types of Romberg integration are referred to as the RI- K methods, with RI-0 corresponding to the composite trapezoidal rule and RI-1 to Simpson's rule. Note that the contour discretization of the polymer is the same for solving the MDEs and evaluating the contour integrals – as the K^{th} RI method requires an integer multiple of 2^K steps along each direction, larger K values place a significant constraint on the allowed values of N_s and, by extension, f_P . All spatial integrals are evaluated using RI-4, constraining the meshes along each direction to be an integer multiple of 16.

In our PSCFPP, methods up to and including $K = 4$ are available to a user to compile the code in. From the perspective of computing phase diagrams, this has the advantage of providing a method to calculate highly accurate solutions via the $K = 3$ and 4 methods that can then be used to benchmark the $K = 0$ and 1 methods. This allows the free energy accuracy to be thoroughly studied and saves a significant amount of memory via lower N_s values at the cost of much fewer available points for a given N_s . The higher-order methods are thus not very suited to mapping out fine phase diagrams in $\{f_P\}$ space while the lower-order methods lend themselves well to this

problem, particularly $K = 1$ for its excellent balance between accuracy and accessibility.

Anderson mixing (AM) is used to update the chemical potential fields – this algorithm has been extensively used in recent SCF calculations in the literature.^{5, 15} With N_m denoting the number of monomer types in the system, N_c the number of cell parameters, and N_f the number of independent degrees of freedom needed to represent the chemical potentials and volume fractions of a monomer, AM's formulation is based on the expression of Eqs. (5), (6), and (8) as a system of $N_m N_f + N_c$ equations.¹⁵ This non-linear system of equations can then be expressed as a requirement that $\mathbf{0} = \mathbf{R}(\mathbf{x})$ where $\mathbf{R}(\mathbf{x})$ is a column vector of $N_m N_f + N_c$ residuals and \mathbf{x} a vector with $N_m N_f + N_c$ elements.¹⁵ The column vector \mathbf{x} contains the field values for all monomer types at every point in the mesh (or for each basis function) as well as the cell parameters – in this way, the error in the SCF equations can be defined as $\varepsilon \equiv |\mathbf{R}(\mathbf{x})|$.¹⁵ In this method, rather than using Eq. (5) to update $\omega_p(\mathbf{r})$ the chemical potentials are recomputed via $\omega_p^{\text{new}}(\mathbf{r}) = \omega_p^{\text{old}}(\mathbf{r}) + \delta\omega_p(\mathbf{r})$, where $\delta\omega_p(\mathbf{r})$ is the update to the field determined by the AM update scheme. The cell parameters are additionally updated in a similar manner at each iteration. The scheme uses past trial values of \mathbf{x} to compute its value at the next iteration and includes the number of histories N_h as a user specified parameter – this refers to the maximum number of past trials that will be used by the AM algorithm.¹⁵ Note that this parameter has no effect on βf_c and simply affects how quickly a solution of the SCF equations at a specified ε is converged on. The Eqs. (5), (6), and (8) then serve as the measure of error rather than the mechanism by which the fields are updated – this measure of error enforces that the solution is self-consistent via Eq. (5), satisfies the incompressibility constraint via Eq. (6), and optimizes the cell parameters via Eq. (8), all simultaneously.

The first step to studying any system with SCFT, regardless of implementation, is to

construct trial fields $\omega_P(\mathbf{r})$ (in real-space) or $\widehat{\omega}_P(\mathbf{k})$ (in reciprocal-space) for all monomer types. PSCFPP favors the latter, performing optimally when trial fields are provided in the symmetry-adapted basis format. The easiest way to obtain a set of trial fields is to use one that is already built into PSCFPP in the ‘examples’ folder, where suitable trial fields for most diblock phases of interest can be found. However, the morphologies that exist near the center of the phase triangle in ABC miktoarms are known to be nothing like the morphologies that form in diblocks, making few of the built in solutions useful to us. Ideally, we would thus like to be able to identify the symmetry group of a morphology of interest and then select the coefficients $\widehat{\omega}_P(\mathbf{k})$ that contribute significantly to its structure – the problem is that it is not obvious which values of \mathbf{k} should be chosen or what their coefficients should be. It is relatively easy, however, to construct $\{\phi_P(\mathbf{r})\}$ for a known morphology and transform it to a suitable set of trial fields $\{\omega_P(\mathbf{r})\}$ via Eq. (5) with $\eta(\mathbf{r}) = 0$. Using PSCFPP, these trial fields can then be expanded in a symmetry adapted basis of one’s choosing to obtain the corresponding $\{\widehat{\omega}_P(\mathbf{k})\}$ that can then be iterated on.

The process used to generate the trial volume fractions for 2D morphologies is discussed here in some detail – these methods are simple to extend to 1D and 3D so as to obtain the L, TPL, and HPL morphologies. All trial fields were created using Python, relying on NumPy arrays to store and manipulate the field data before writing to a text file in the format PSCFPP reads. A 2D morphology formed by a neat melt of ABC miktoarm terpolymers is described by a set of three volume fraction fields, one for each type of monomer. Only two of these fields are independent owing to the incompressibility constraint Eq. (6) – in all cases, we create $\phi_P(\mathbf{r})$ for $P = A, B$ and compute $\phi_C(\mathbf{r})$ from Eq. (6). To create competent trial fields for particle forming phases in SCFT it is generally sufficient to place simple geometric objects (cylinders, spheres, tetrahedra) at the corresponding locations of concentrated regions in the morphology of interest. An ‘object’ in this

context is a field that varies between 0 and 1 such that it captures a desired geometry – an example of this for a cylinder in 2D is shown in Fig. 2.1. This object was created using a simple analytic function $c(x, y)$ given by

$$c(x, y) = \frac{1}{4}(1 - \cos x)(1 - \cos y) \quad (18)$$

where x and y correspond to the horizontal and vertical directions, respectively, and are both bounded by 0 and 2π . By controlling the number of grid points along each direction, the radius of the resulting cylinder can be specified freely. This allows cylindrical domains of arbitrary size to be placed at arbitrary locations in a 2D array using array operations, forming the basis of the methods used to create trial fields in this study. First, two meshes corresponding to $\phi_A(\mathbf{r})$ and $\phi_B(\mathbf{r})$ are created whose aspect ratio approximately matches that of the trial cell parameters – all field values are initially set to zero. Cylindrical domains are then placed at the appropriate regions

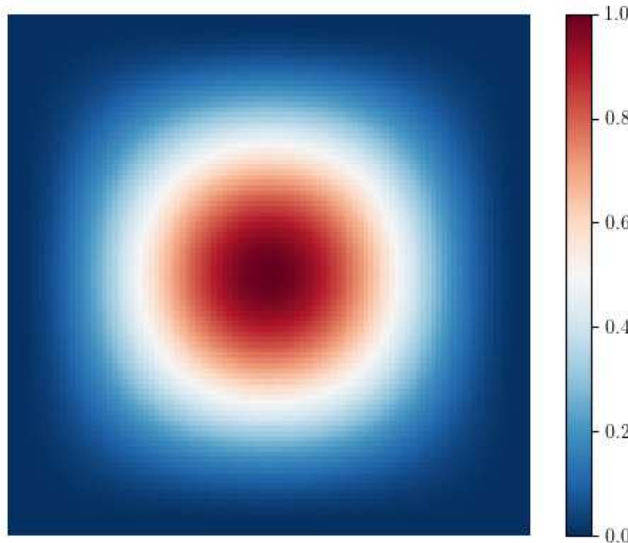


Figure 2.1 Cylinder motif generated with a 100x100 mesh, used to create 2D trial volume fraction fields.

for a morphology of interest by using Eq. (18) and explicitly inserting them with array operations. Once this has been completed for $\phi_A(\mathbf{r})$ and $\phi_B(\mathbf{r})$, $\phi_C(\mathbf{r})$ is then computed via $1 - \phi_A(\mathbf{r}) - \phi_B(\mathbf{r})$. The trial fields $\omega_P(\mathbf{r})$ are then calculated (for a specified χN) via

$$\omega_P(\mathbf{r}) = \chi N \sum_{P' \neq P} \phi_{P'}(\mathbf{r}). \quad (18)$$

These fields are then written to a text file in the appropriate format for PSCFPP to interpret them. This approach is not limited to 2D, for 3D morphologies can also be considered as a set of 3D arrays – for example, spherical domains analogous to that shown in Fig. 2.1 can be created through the incorporation of a term that depends on z to Eq. (18). These can then be placed at arbitrary locations in 3D space to create trials fields suitable for the two 3D phases considered in this study, although whether techniques like this could be used to create trial fields for more complex 3D morphologies remains to be seen.

In order to interface completely with PSCFPP it is necessary to have methods available for creating trial fields, encoding/decoding text files, and visualizing results – additionally, if one wishes also to compute thermodynamic information from outputs such as $\{\omega_P(\mathbf{r})\}$, $\{\phi_P(\mathbf{r})\}$ or $\{q_P(\mathbf{r}, s)\}$ then a high-accuracy multi-dimensional numerical integration technique must be available. As PSCFPP does not have any of these capabilities accessible to a user, Python based methods were developed capable of creating trial fields in real-space, reading and writing text files in real-space for the chemical potential/volume fraction fields, plotting fields of interest in any dimension (though the 3D methods are still somewhat immature), and computing 1D/2D integrals numerically for any specified field using RI-4. These methods are at a level such that they can dramatically simplify the task of further study on ABC miktoarms with PSCFPP by providing the basic tools necessary to obtain, interpret, and analyze outputs from SCFT. The 3D methods, while

perfectly functional, are in some need of refinement and the code is not general enough to allow use for arbitrary systems in PSCFPP – methods generally only work for files corresponding to three-component systems and some diblock phases.

Finally, we note that all of the converged SCF results from this study including $\{\hat{\omega}_P(\mathbf{k})\}$ files for all morphologies are stored in corresponding folders in a PSCFPP install. This data, were it to be incorporated into the distributed version, would provide an immensely useful basis for studying ABC miktoarm terpolymers, much as the included diblock examples have made studying diblock copolymer phases with PSCFPP vastly simpler. It would also make replicating the results obtained here trivial, something many SCF studies have not provided.

Chapter 3: Results

This chapter is divided into three sections – section I, Numerical Accuracy, discusses the effects that need to be accounted for (both physical and numerical) in order to compute high-accuracy SCF solutions and presents the results of a detailed free energy study for (3.3.4.3.4) and TPL. Section II, Phase Diagram, details how a composition phase diagram (at constant χN) is computed within SCFT of the ‘standard’ model for a neat melt of ABC miktoarms using the REPS-K methods, with the corresponding central region of the phase diagram mapped out for $\chi N = 30$. Section III, Free Energy and Stability Analysis, presents the relative Helmholtz free energies of all morphologies along the $f_B = f_C$ isopleth and decomposes them into their entropic and energetic contributions (as described in Chap. 2.1) to explain their stability; the same is done for all morphologies at a point $f_A = 0.45$, $f_B = 0.30$ where (3.3.4.3.4) is shown to be stable, with their entropic and energetic contributions decomposed further into the contributions of each species and the junctions.

I. Numerical Accuracy

All calculations were done on an NVIDIA A100 GPU with ~20 GB of available memory. The numerical parameters necessary to achieve high accuracy in βf_c resulted in 2D jobs requiring 1-5 GB of memory while 3D jobs generally required at least 10 GB. By ‘accuracy’ we mean the number of decimals that the quantity in question has been computed to – for example, an accuracy of 10^{-3} would mean that the quantity is known to three decimals or equivalently that the error is on the order of 10^{-4} . The memory required to store the information necessary for an SCFT solution, such as $\{\hat{\omega}_P(\mathbf{k})\}$, $\{q_P(\mathbf{r}, s)\}$, etc., scales heavily with the contour discretization N_s and spatial discretization $\{m_d\}$ where m_d denotes the number of intervals along any direction d – recall

that RI-4 is used to evaluate all spatial integrals such that m_d must be an integer multiple of 16. The accuracy of the Helmholtz free energy also depends strongly on these parameters, and one would like to minimize the amount of memory used while simultaneously maximizing the accuracy of βf_c . This accuracy has a limit set by the tolerance ε that the SCF equations are solved to – as the free energy Eq. (7) depends on $\{\omega_P(\mathbf{r})\}$, $\{\phi_P(\mathbf{r})\}$, and Q it is only possible to resolve it to the accuracy that these quantities are resolved. It is thus necessary to study the effect of N_s and $\{m_d\}$ before making any definitive statements on values of βf_c . The results of this accuracy study are presented first as these results guide the numerical parameter values used in constructing the phase diagram and computing any other quantities of interest.

The test phases to conduct the study described here are chosen as (3.3.4.3.4) and TPL for their complexity and relatively large unit cells, with (3.3.4.3.4) having the largest cell parameters of any phase – see Table 3.1. This table gives the optimal cell parameters minimizing βf_c of the

Table 3.1 Optimized cell parameters (in units of R) and symmetry groups for all morphologies at $\chi N = 30$, corresponding to the unit cells shown in Fig. 1.2 and listed in order of magnitude. The third parameter for TPL and HPL shows the size of the parameter perpendicular to the faces with four and six-fold symmetries, respectively.

[6.6.6]	[8.8.4]	[8.6.4;8.6.6]	[10.6.4;10.6.6]	[12.6.4]	(3.3.4.3.4)	L	L+C	TPL	HPL
p3m1	p4mm	p2mm	pm	p6mm	p4mg	P $\bar{1}$	p2mm	P422	P622
1.51960	2.16825	1.54515	1.98084	1.94496	3.40297	1.58145	1.03212	1.42649	1.24586
2.71162	2.16825	3.35042	3.05146	1.94496	3.40297	-	1.44020	1.42649	1.24586
-	-	-	-	-	-	-	-	1.55455	1.49674

corresponding phase at block fractions where each is stable with the exception of the metastable TPL, as well as the symmetry group of each morphology in standard Hermann-Mauguin notation.

The cell parameters of any morphology are, in general, sensitive to the block fractions $\{f_P\}$ as well as the degree of segregation χN though the values provided here would serve as suitable trial values near any phase's region of stability – in practice, provided the trial fields are reasonably good then the trial cell parameters do not need to be exceptionally close to their optimal values. The symmetry groups associated with each phase specify the set of basis functions the trial fields are expanded in – note that since a rectangular unit cell is used for [6.6.6] it is expanded in a pm basis rather than p3m1. This is because PSCFPP associates a p3m1 basis with a hexagonal unit cell – if a rectangular unit cell is to be used, a symmetry-adapted basis associated with a rectangular cell must also be used. Other than requiring a larger mesh than the corresponding hexagonal unit cell to achieve the desired free energy accuracy this has little consequence on calculations, the only notable difference being that more basis functions are required to represent the morphology than would be with p3m1.

To study the free energy accuracy of (3.3.4.3.4), Eq. (7) was evaluated repeatedly for the unit cell shown in Fig. 1.2 at $f_A = 0.45$, $f_B = 0.30$, and $\chi N = 30$ by systematically varying the contour discretization $N_s \in [64, 448]$, spatial discretizations $m_d \in [16, 512]$, and numerical order $K \in [1, 4]$. As (3.3.4.3.4) has a square unit cell the discretizations along the x and y directions are the same, i.e., $m \equiv m_x = m_y$. We define the error Δ of $\beta f_c(N_s, m, K)$ as

$$\Delta(N_s, m, K) \equiv \beta f_c(N_s, m, K) - \beta f_c^* \quad (19)$$

$$\beta f_c^* \equiv \beta f_c(N_s^{\max}, m^{\max}, K^{\max}). \quad (20)$$

This quantity can then be computed at every set of numerical parameters and compared to see what values are necessary to achieve the desired accuracy. By Eq. 20, βf_c^* is simply the most accurate available value for the free energy – in all cases we take $\beta f_c^* = \beta f_c(N_s = 448, m = 512, K =$

$4) = 8.43668488$. As the values of the cell parameters also affect the value of βf_c , they must be held constant during the accuracy study. This was accomplished by first computing a solution to the specified tolerance of $\varepsilon = 10^{-8}$ while allowing the cell parameter to be optimized, then using the optimal values held constant for all subsequent calculations. All computations used the same trial fields $\{\hat{\omega}_P(\mathbf{k})\}$ obtained from an already converged (3.3.4.3.4) solution such that the only variance between jobs was the numerical parameters whose effect was being studied.

The results are shown in Fig. 3.1 for $K = 1$ and $K = 4$ to highlight the memory savings that can be gained from larger K , where REPS-4 allows nearly 10^{-7} accuracy in βf_c with only

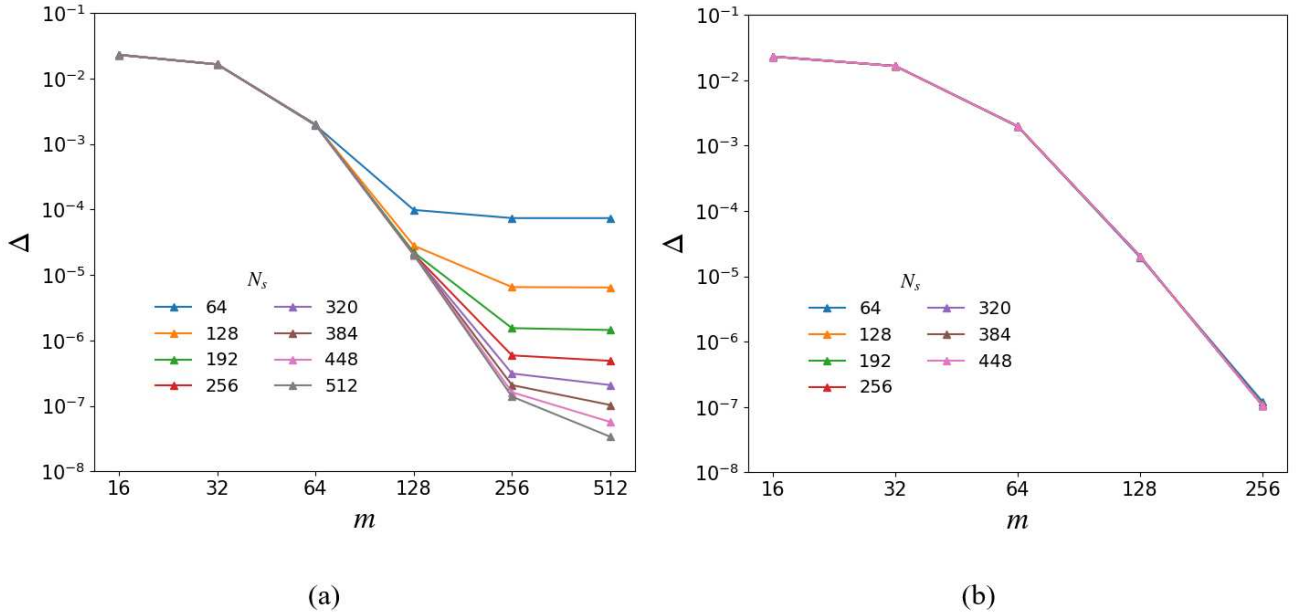


Figure 3.1 Log-log plot of βf_c error data for (3.3.4.3.4) and various N_s at $\chi N = 30$ with (a) $K = 1$ and (b) $K = 4$.

$N_s = 64$ and $m = 256$ while REPS-1 yields barely 10^{-4} accuracy at the same discretizations. Figure 3.1b clearly shows the collapse of all curves, indicating that the contour discretizations considered are large enough such that the error is controlled solely by the mesh discretization m

with REPS-4. We note that with a method such as REPS-1 (equivalent to the fourth-order pseudospectral method) in Fig. 3.1a, the error is largely controlled by the spatial discretization up until $m \approx 128$ at which point the inaccuracies from the contour discretization become apparent. It is at this point that the curves flatten out with respect to m , indicating that the accuracy is being limited by N_s , while the N_s curves themselves can be seen to collapse to the same as that in Fig. 3.1b as $N_s = 512$ is approached. This indicates the fundamental resolution of the numerical methods used, where it is clear that relatively large parameters must be used to obtain results of high accuracy.

The study on TPL was carried out in a similar manner at $f_A = 0.50$, $f_B = 0.30$, and $\chi N = 30$ near where it is a competitor in the phase diagram. In this case the SCF equations were solved to a tolerance of $\varepsilon = 10^{-6}$ but the procedure was otherwise identical, with less total numerical parameters considered for simplicity. Here we took $\beta f_c^* = \beta f_c(N_s = 80, m = 112, K = 3) = 8.161733$ and a cubic mesh of total discretization m^3 with the results shown in Fig. 3.2. This again highlights the resource savings that can be achieved with the higher- K methods, something particularly important for 3D phases owing to their large computational costs. In this case, it is possible to achieve contour saturation with only $N_s = 80$, allowing mesh accuracy to be pushed further. While this is less important at smaller degrees of segregation such as $\chi N = 30$, larger degrees of segregation increase the computational cost of obtaining a solution with the same accuracy dramatically, making memory-efficient options more appealing. In fact, owing to the large computational costs of the REPS- K methods and the current amount of available GPU memory on the server used, it is likely that high-accuracy computations would be impossible with $K = 1$ at stronger segregations. Larger K would have to be used, which would then limit the resolution of the phase diagram significantly – to avoid this, more memory would have to be

available or a less resource intensive solution method used, such as the spectral method. In this work, only $\chi N = 30$ is considered in phase-space such that these results are sufficient for our purposes, though this must be kept in mind for future studies of this system with PSCFPP.

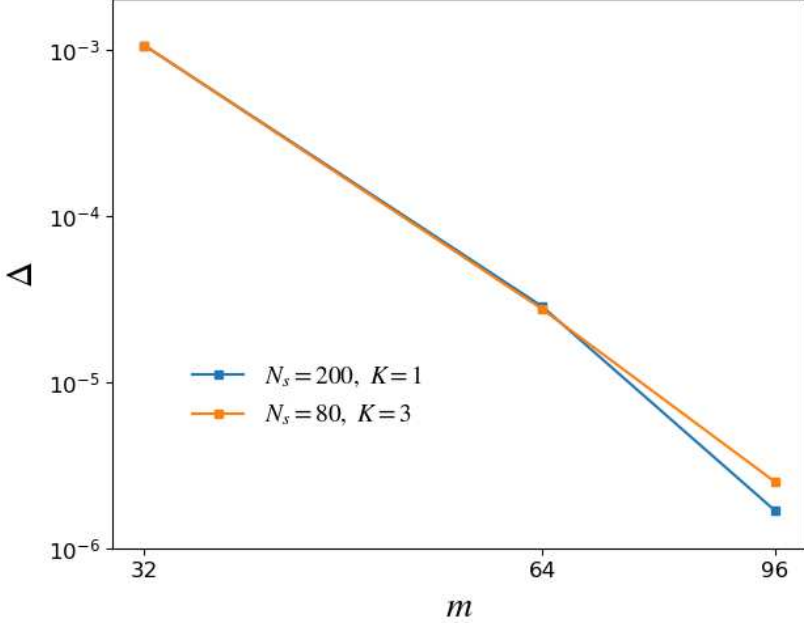


Figure 3.2 Log-log plot of βf_c error data for TPL at $\chi N = 30$ with $K = 1$ and 3.

II. Phase Diagram

To achieve the goal of computing high-accuracy SCF results for a neat melt of ABC miktoarms at $\chi N = 30$ we choose a standard tolerance of $\varepsilon = 10^{-5}$ in all the following results. This means that the maximum accuracy one can resolve βf_c to for any morphology is 10^{-5} or 5 decimals, dependent on using contour and spatial discretizations large enough to ensure convergence. When choosing these other numerical parameters that are to be used in computing phase data, the first parameter to set is that of K as it specifies both the βf_c accuracy that will be obtained and the number of accessible points in the phase diagram for any given N_s . This second

constraint is equivalent to setting the resolution one can achieve in $\{f_P\}$ space – with $K = 0$ or 1 the contour discretizations N_s and $\{N_p\}$ are constrained to be integer multiples of 1 or 2 , respectively. In practice this means that both methods have a large number of points available to them for any allowed N_s , although we note that for $K = 0$ the discretization $N_s = 100$ yields access to all points $\{f_P\}$ describable by 2 decimals (i.e., $0.40, 0.41, 0.42$, etc.) for any f_P . The same points are available with $K = 1$ at a contour discretization of $N_s = 200$, and for $K = 2$ at $N_s = 400$. For $K > 1$ the value of N_s necessary to allow access to these points is too large, particularly considering the higher computational cost per contour step and extreme accuracy of these methods. For $K = 1$, however, $N_s = 200$ is not prohibitively large and further allows an accuracy of 10^{-5} in βf_c to be easily obtainable with the appropriate spatial discretizations for both (3.3.4.3.4) and TPL, via Figs. 3.1 and 3.2. The combination of these qualities makes the choice of $K = 1, N_s = 200$ an optimal one for the construction of the phase diagram at $\chi N = 30$, and so these parameters are used for all morphologies to obtain all of the following results.

For any given morphology, the final numerical parameters left to specify are the spatial discretizations $\{m_d\}$ which simply need to be chosen so as to match the 10^{-5} accuracy in βf_c afforded by the other quantities. Based off Figs. 3.1 and 3.2, we choose $m = 256$ and $m = 96$ for (3.3.4.3.4) and TPL, respectively, both being large enough to guarantee 10^{-5} accuracy. For other morphologies, we use these spatial discretizations as guidelines and are careful to ensure that 10^{-5} accuracy in βf_c is always retained. In practice, the 3D morphologies (TPL and HPL) always use $m = 96$ while the discretizations for the 2D morphologies along any direction d are $m_d \geq 192$. The sole 1D morphology L is always computed with $m = 512$. To construct the phase diagram for the system at $\chi N = 30$, we compute βf_c for each morphology at each point in block fraction space afforded by the chosen K and N_s and compare the values. The stable morphology at any

point is selected as that having the lowest βf_c . We focus our calculations on finding all of the points in the region of the phase diagram considered that bracket phase boundaries between the various morphologies, as these are what specify the structure of the phase diagram. For all computations the unit cell parameters are allowed to be optimized via PSCFPP's built-in algorithm, and the constructed phase diagram is shown in Fig. 3.3. Note that symmetric interaction parameters reduce the area that calculations need to be done for to 1/6 that of the total phase diagram – the rest of the phase diagram can be generated from this triangular region by reflection

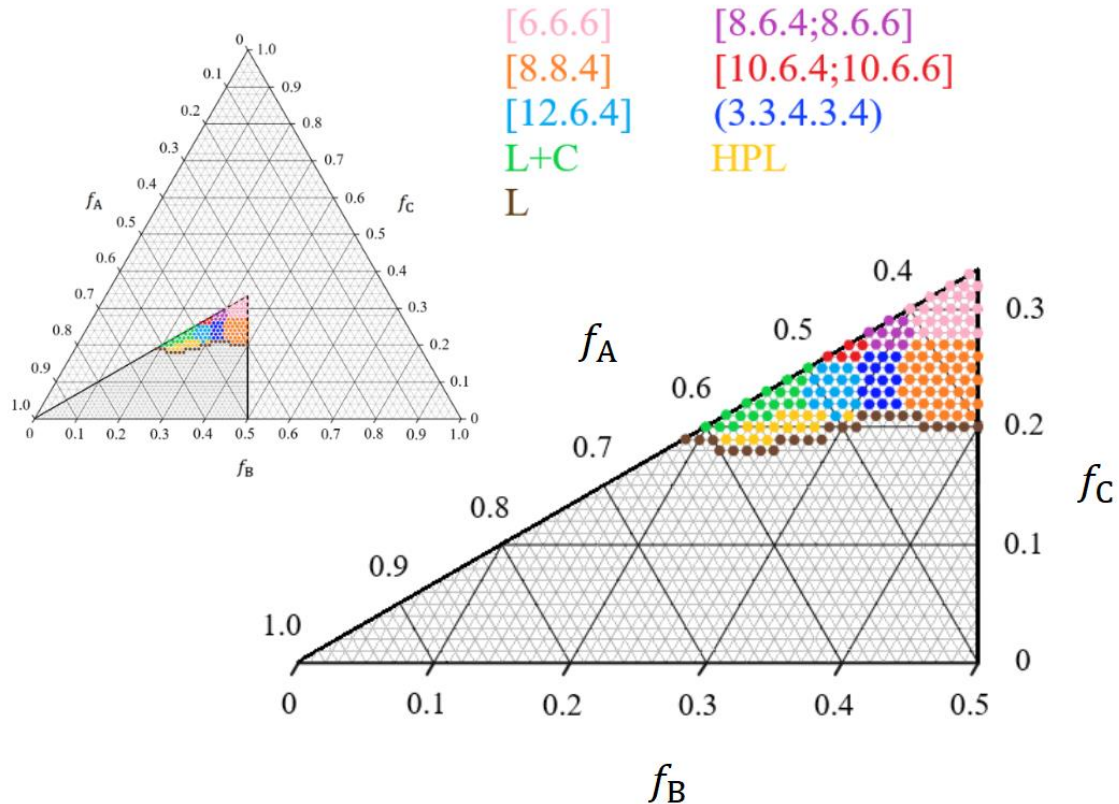


Figure 3.3 Phase diagram for a neat melt of ABC miktoarms at $\chi N = 30$. Calculations are done at points that bracket phase boundaries, with the interior regions of each phase filled in for clarity of visualization.

across the various isopleths. In this computed region, we have $f_A > f_B > f_C$ except for the $f_B = f_C$ isopleth that forms the hypotenuse and the $f_A = f_B$ isopleth bounding the region to the right. The underlying grid in the triangle shows every $\{f_P\}$ where calculations can be done with $N_s = 200$ and $K = 1$, the available points being located at the intersections of lines. The colored dots overlaid at various points denote the phase found to be stable at that point with different colors corresponding to different morphologies.

The most notable results are the regions of stability of [10.6.4;10.6.6], [12.6.4], (3.3.4.3.4), and HPL; this is the first time the HPL phase has been reported as stable. By definitively computing βf_c to 10^{-5} accuracy and observing that the smallest difference in βf_c between any two phases is on the order of 10^{-5} we leave no question as to the stability of the presented morphologies, thus resolving the discrepancies brought about by the differences in results of Refs. 12 and 17. This further provides proof that (3.3.4.3.4), [12.6.4], and [10.6.4;10.6.6] do not enter into the diagram at larger χN but are present at smaller values, and most likely always play a significant role regardless of the degree of segregation based off the similarity with the results computed in Ref. 18 at $\chi N = 60$. It is interesting to note that the general structure of the phase diagram computed here at $\chi N = 30$ is nearly identical to that of Ref. 18 (shown in Fig. 1.4a), excepting the presence of HPL which was not included in their calculations. Based off these results it would appear that the stable regions of all phases become elongated and occupy a larger area as χN is increased, with the effect becoming more pronounced the farther away from the center one is. For example, we find L+C to be stable up until $f_A = 0.6$ on the $f_B = f_C$ isopleth, past which point lamellae L becomes stable at $\chi N = 30$. At $\chi N = 60$, however, Ref. 18 finds the stable region of L+C to extend out to nearly $f_A = 0.8$ along this isopleth with L notably not found near this region. It is possible that the stable region of L shrinks significantly as χN is increased, owing to the constraint

that the miktoarm topology places on this morphology of having the shortest C arms constantly in contact with A and B arms – this would result in prohibitively large internal energy at stronger segregations. The [12.6.4] phase additionally occupies a much larger region in Fig. 1.4a, extending out to nearly $f_A = 0.6$ rather than $f_A \approx 0.5$ as we find in this study; however, Ref. 18 did not consider HPL which is the phase we find to dominate this region. The phases closer to the center of the diagram occupy similar regions in both studies, being shifted minorly in Fig. 1.4a relative to those shown in Fig 3.3 – it would thus appear that while stronger segregations may cause phase boundaries to shift significantly they do not result in the appearance (or disappearance) of phases near the center of the diagram, though further research is necessary to confirm this for morphologies such as HPL. As this is largely the case for diblock copolymers, it would be fitting for the same phenomenon to be at play in ABC miktoarms – not enough is known to definitively conclude this, however.

Upon comparison with the results of Ref. 17 in Fig. 1.3a the agreement is generally quite good, with the exception of the [12.6.4] and [8.8.4] phases. The stable region of [8.8.4] is presented as much larger than that in Fig. 3.3b because Ref. 17 did not consider (3.3.4.3.4), leading to the area of [8.8.4] being overestimated. Based off our results, [12.6.4] occupies a significantly larger region than that shown in Fig. 1.3a, though we did not consider the possible existence of the [8.6.4;8.8.4;12.6.4;12.8.4] phase. While this phase has not been reported in any other studies on ABC miktoarms, that does not mean that it should be ignored – to justify its inclusion in future work, we note the presence of an anomaly in our results. In Fig. 3.3b, at $f_A = 0.49$ and $f_B = 0.3$ we find HPL to be stable at a single point outside of its nominal stable region. We do not believe that this is a mistake – the free energy difference between HPL and competing phases is on the order of 10^{-3} , well within the accuracy of this study. Rather, this result suggests that another phase

is probably stable here, one that was not included in our computations. Ref. 17 finds [8.6.4;8.8.4;12.6.4;12.8.4] to have a very small region of stability in the direct vicinity of this point – it is possible that this atypical tiling pattern is a stable phase here, and has not been observed elsewhere because of the small area it occupies in the phase diagram. It is also possible that other morphologies not considered in this work play a role here, including the [8.6.4;8.6.6;12.6.4] tiling pattern reported in Ref. 18 or one of the other possible 3D morphologies reported in Ref. 12.

III. Free Energy and Stability Analysis

A great deal of information about morphologies and their stability can be extracted from the Helmholtz free energy per chain and its decompositions. To study this, the dimensionless Helmholtz free energy per chain for all candidate morphologies is shown as a function of f_A along the $f_B = f_C$ isopleth in Fig. 3.4. Note that the composition is specified solely by f_A along this isopleth, and all values are taken relative to that of the L+C phase (with βf_c^R denoting a reference

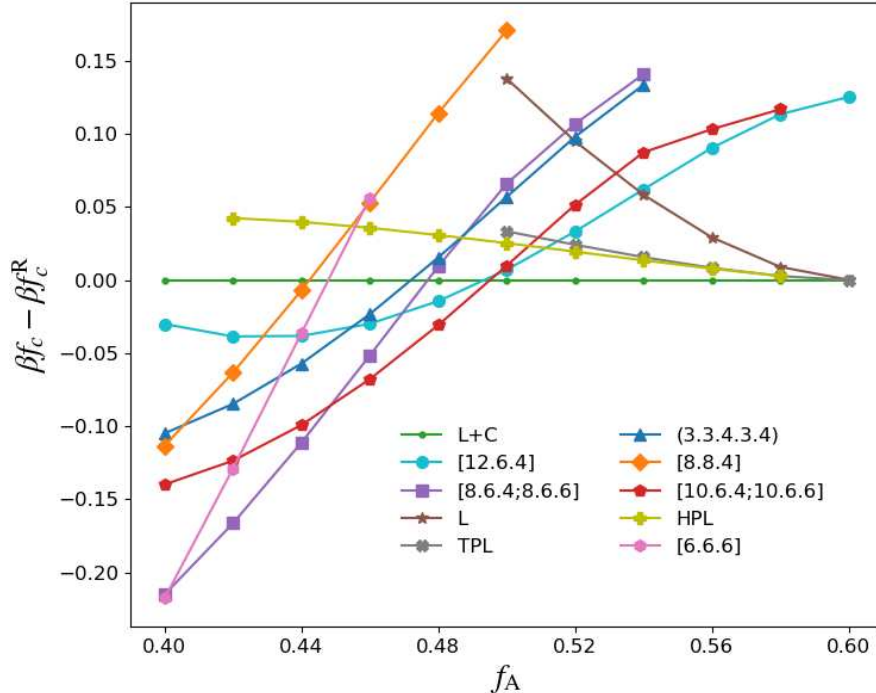


Figure 3.4 Free energy data relative to L+C along the $f_B = f_C$ isopleth.

free energy of phase R). Increasing f_A in Fig. 3.4 corresponds to moving out from $f_A = 0.4$ along the isopleth in Fig. 3.3, where there is a transition from tiling patterns to lamellae-based phases as one moves along this isopleth that is indicative of the general trend observed in ABC miktoarms. Additionally, [12.6.4] is found to be metastable at every point along the isopleth – the fact that Fig. 1.4c shows [12.6.4] occupying a relatively large region of this isopleth further supports the trend that stronger segregations widen the stability region of phases near the center of the diagram. Considering the lamellae-based morphologies, we note that TPL has only slightly higher βf_c than HPL – this is consistent with the general trend observed for these morphologies, where their βf_c are close to degenerate with HPL always being slightly (on the order of 10^{-3}) lower than TPL. Further, the free energies of the four lamellae-based phases appear to converge to the same value at $f_A = 0.6$; at this point it is found that regardless of the trial field used for these phases, all morphologies will converge on L except L+C which retains some two-dimensional character. L+C also retains the lowest βf_c at this point, although L (and thus the other phases) have values only $\sim 10^{-4}$ higher. Fig. 3.4 also informs us that the free energy of a morphology whose stable region is relatively far from the isopleth, such as [8.8.4], will be significantly higher than morphologies that lie closer to it in the phase diagram. This trend is valid for any phase that is computed at a point far from where it is stable, and allows the list of candidate phases to be adjusted depending on where in the phase diagram computations are being done.

By using the decomposition of βf_c given by Eqs. (9) and (10) in Chap. 2.1 it is possible to study the thermodynamic effects that govern each phase's stability. These quantities are shown for every phase along the $f_B = f_C$ isopleth in Fig. 3.5, where we notice two general trends: the tiling patterns are consistently able to achieve lower dimensionless internal energy per chain βu_c than the lamellar phases at the cost of lower dimensionless entropy per chain s_c/k_B , while lamellar

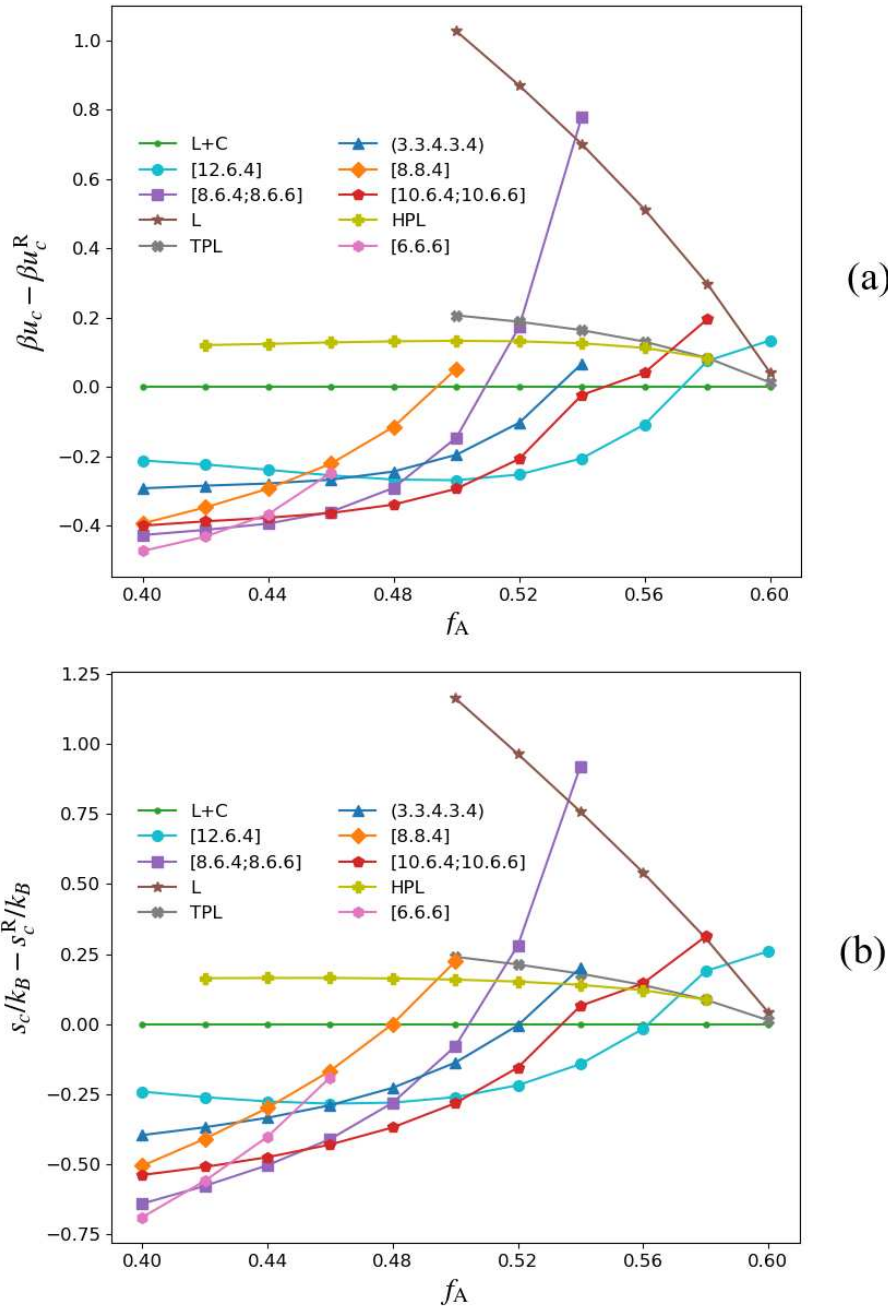


Figure 3.5 Decomposed free energy data relative to L+C along the $f_B = f_C$ isopleth, with (a) internal energy per chain and (b) entropy per chain for each morphology.

phases are more easily able to maximize their s_c/k_B at the cost of higher βu_c . Near the center of the phase diagram at $f_A = 0.4$, [6.6.6] achieves its stability by having the lowest βu_c of competing

phases, though it also has the lowest s_c/k_B . The [8.6.4;8.6.6] and [10.6.4;10.6.6] morphologies are similarly energetically stabilized at the next four points along the isopleth as they retain both the lowest s_c/k_B and βu_c of any phase. At $f_A = 0.5$ L+C becomes stable, and has somewhat unique behavior – it neither manages to minimize its βu_c or maximize its s_c/k_B relative to the other phases. However, it combines the beneficial effects of both the tiling patterns and lamellar phases as it is able to attain lower βu_c than any other lamellar phase while also achieving higher s_c/k_B than any of the tiling patterns. The combination of these effects serves to stabilize L+C until $f_A > 0.6$ at which point L is able to lower its βu_c enough to become stable.

The results in Fig. 3.5 also serve to explain the general trend of tiling patterns into lamellar phases as one progresses outward in the phase diagram. From visualizing the morphologies at each point along the isopleth, it is observed that as f_A is increased, the largest cylindrical domains (in red in Fig. 1.2) in the tiling patterns become swollen, forcing the smaller B and C blocks to mix together in a disordered matrix surrounding the A domains that are still highly pure. This forced transition to a pseudo-disordered morphology occurs for all tiling patterns as f_A is increased, and has a large energetic cost due to the mixing of B and C segments as can be seen in Fig. 3.5a. As the mixing is entropically favorable, this phenomena is accompanied by an increase in entropy of the affected morphologies, though it is not enough to outweigh the energetic penalty. The transition to lamellar phases occurs because these morphologies are capable of significantly reducing βu_c relative to the tiling patterns while simultaneously affording the system a reasonable s_c/k_B , nearly competitive to the tiling patterns. These results serve to highlight the delicate balance between entropic and energetic effects at play in microphase-separated BCPs, where subtle differences in parameters can drive the formation of completely different phases.

We turn now to studying the (3.3.4.3.4) tiling pattern in more depth. This morphology is

interesting for a number of reasons – it is an example of a cylindrical Frank-Kasper σ phase, with its structure being the same as a cross-section of the spherical σ phase formed via conformational asymmetry in neat diblock melts.⁵ Theoretical calculations¹¹ have shown that the morphology could potentially exhibit photonic band gaps with the appropriate dielectric contrast, and the frequent experimental observations of it^{10, 21} (in addition to the results of Fig. 3.3b) show that it plays a prominent role in neat melts of ABC miktoarms. To understand more about this morphology and what effects drive its stability over competing phases, we present a detailed breakdown of βf_c for (3.3.4.3.4) and its adjacent tiling patterns, as well as L+C and L. This analysis is conducted at a point where (3.3.4.3.4) is known to be stable, $f_A = 0.45$ and $f_B = 0.3$, and is based on the decomposition given by Eqs. (14)-(16) where we compute each of these quantities for every species at the point of interest.

To carry out these computations it is necessary to know the junction density $\rho_J(\mathbf{r})$ for each morphology, given by Eq. 11 – this field is of some interest itself as well, as it provides information about how the polymers are distributed throughout a morphology. From the plots given in Fig. 1.2, we would expect the junctions to be located primarily at the intersections of the majority regions of each component – Fig. 3.6 shows $\rho_J(\mathbf{r})$ in a unit cell of (3.3.4.3.4) at $f_A = 0.45$ and $f_B = 0.3$, which confirms this expectation. However, there is a surprising amount of networking present from the junctions which can be attributed to the value of $\chi N = 30$ this field was obtained for. As χN is increased, this networking should diminish significantly until the junctions are concentrated along nearly one-dimensional lines perpendicular to the page at strong segregations. It is clear, though, that at $\chi N = 30$ considered here the junctions are smeared along interfaces rather than tightly aligned. The same features are observed in general for all morphologies, with the junctions being smeared out in space while concentrated at vertices. Note that the lamellae-based phases are

observed to have junction densities that occupy a relatively larger area than the tiling patterns – this effect is quantified by the translational entropy of the junctions, discussed next.

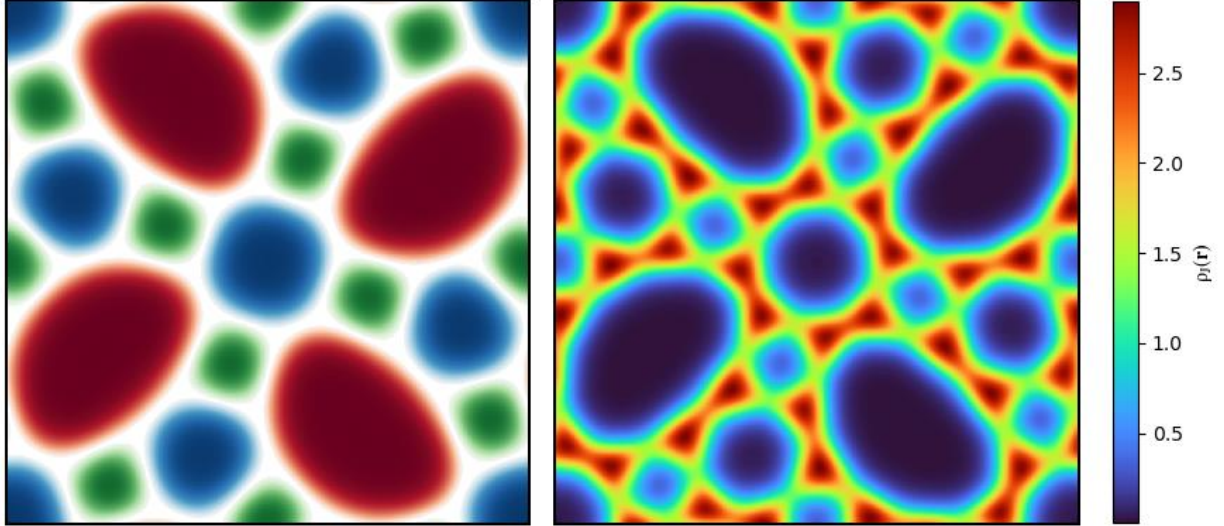


Figure 3.6 Unit cell of (3.3.4.3.4) (left) and the corresponding junction density (right) at $\chi N = 30$, $f_A = 0.45$, $f_B = 0.3$.

Table 3.2 shows the results from computing the quantities in Eqs. (14)-(16) for (3.3.4.3.4) and the tiling patterns it shares a phase boundary with as well as two lamellar phases, L+C and L. Comparing the tiling patterns first, the rectangular patterns [10.6.4;10.6.6] and [8.6.4;8.6.6] are able to achieve the lowest βu_c though they accomplish this at the cost of the lowest s_c/k_B , as discussed earlier for the phases along the $f_B = f_C$ isopleth. The [8.8.4] and [12.6.4] patterns, on the other hand, are able to maximize their s_c/k_B at the cost of βu_c . (3.3.4.3.4) is uniquely able to balance these effects, achieving a βu_c nearly as low as the rectangular patterns while simultaneously achieving an s_c/k_B nearly as large as [8.8.4] and [12.6.4]. This can be attributed to the conformational flexibility that (3.3.4.3.4) allows the C block as well as the low AB internal energy the morphology is able to achieve, as can be seen from the corresponding rows in Table

Table 3.2 Decomposed βf_c data for (3.3.4.3.4) and competing phases at $\chi N = 30$, $f_A = 0.45$, $f_B = 0.3$. Each row denotes the contribution of those species to the italic quantity above it.

	(3.3.4.3.4)	[8.8.4]	[12.6.4]	[10.6.4;10.6.6]	[8.6.4;8.6.6]	L+C	L
βu_c	4.62002	4.68395	4.68162	4.60643	4.59868	5.07278	5.41406
AB	1.21134	1.20735	1.19534	1.39535	1.46051	1.41849	0.92110
AC	1.64591	1.82221	1.52808	1.40143	1.47382	1.70098	2.06061
BC	1.76276	1.65438	1.95818	1.80964	1.66433	1.95330	2.43234
s_c/k_B	-3.91944	-3.89073	-3.88175	-3.96457	-3.97515	-3.56498	-3.31928
A	-1.51044	-1.40509	-1.59980	-1.56810	-1.46112	-1.37736	-1.47539
B	-1.18885	-1.27493	-1.09454	-1.05174	-1.12823	-1.05246	-1.10202
C	-0.81770	-0.81392	-0.78268	-0.94289	-0.99236	-0.80373	-0.37544
J	-0.40244	-0.39678	-0.40472	-0.40182	-0.39343	-0.33141	-0.36641

3.2. The conformational entropy of the C block in (3.3.4.3.4) is significantly greater than that allowed by the rectangular morphologies, while its AB internal energy is also much lower. This is balanced by relatively large AC and BC internal energies, although the morphology is still able to achieve lower values here than [8.8.4] and [12.6.4]. Similar to L+C along the $f_B = f_C$ isopleth, (3.3.4.3.4) thus achieves its stability by being the morphology that achieves the greatest compromise between energetic and entropic effects.

It is interesting to note that, with the exception of [8.8.4], the largest interaction energies for all morphologies come from the BC monomer overlaps. This is most likely due to the fact that shorter blocks (B and C in this case) are allowed higher mobility in a given morphology at lower segregations, and can thus spread out more in space resulting in more unfavorable contacts with the other minority blocks. This is further supported by the majority blocks having the smallest interaction energies for all morphologies. Another notable result is that there is little difference in the translational entropy afforded the junctions of each tiling pattern – considering the translational

entropies of the lamellae-based junctions, this appears to be a distinguishing feature between the two classes of morphology. The lamellar phases can be seen to have significantly larger $s_{c,J}/k_B$, especially L+C which maximizes this quantity relative to the other phases – this would suggest the miktoarms in this morphology are highly distributed in space, or networked. By observing the density $\rho_J(\mathbf{r})$ in Fig. 3.7 it can be seen that this is indeed the case, with the miktoarms showing a strongly 2D distribution along the interfaces. As expected, L+C and L both have prohibitively high βu_c at this point in $\{f_P\}$ space while simultaneously having much higher s_c/k_B than any of the tiling patterns. This is in part owed to the greater $s_{c,J}/k_B$ afforded these phases, but has a more significant contribution from the increased $s_{c,P}/k_B$ the lamellar phases attain for all blocks. L in particular manages to achieve an enormous amount of $s_{c,C}/k_B$, but as discussed it does this at even higher energetic costs.

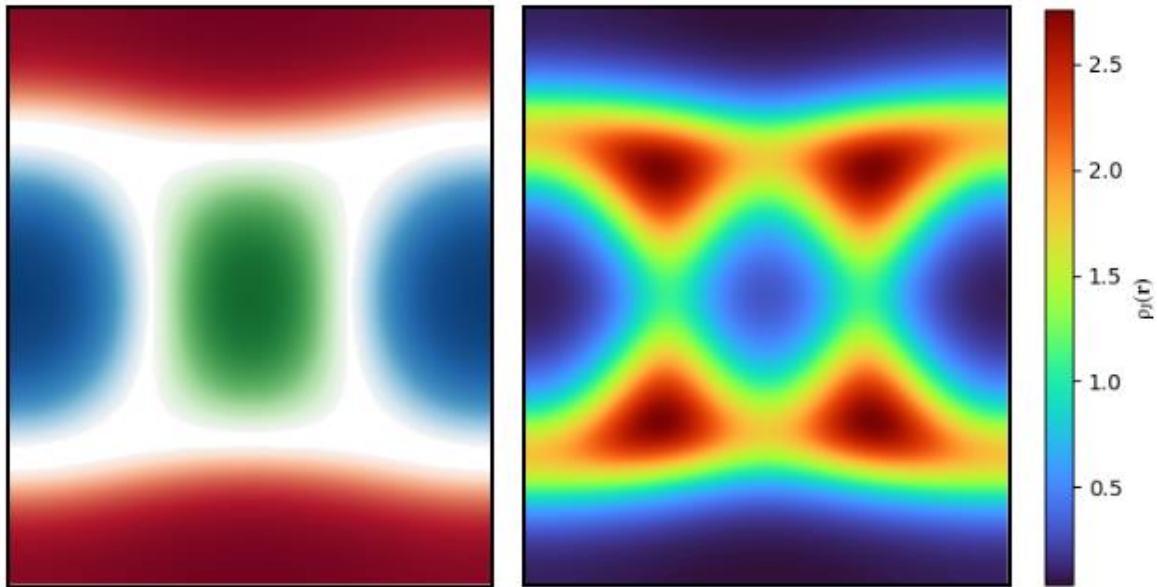


Figure 3.7 Similar to Fig. 3.6 but for L+C.

Chapter 4: Conclusions

In this work, the phase behavior of symmetrically interacting ABC miktoarm terpolymers was studied with self-consistent field theory (SCFT) using an open-source software, PSCFPP, to implement the requisite numerical methods. The numerical error in the results was rigorously studied to ensure that 5 decimals of accuracy were obtained in the dimensionless Helmholtz free energy per chain, and the center of the ternary phase diagram was mapped out at $\chi N = 30$ by considering ten candidate morphologies including six 2D tiling patterns and two 3D phases. Discrepancies in the literature concerning the stability of a number of 2D phases were resolved, and a 3D phase previously found to be metastable was identified as a prominent stable phase. Free energy data was analyzed for various morphologies to understand what drives their stability, and some properties of (3.3.4.3.4) were investigated including the distribution of the miktoarm junctions.

The morphologies included in our calculations were based on those known to play a significant role from previous theoretical and experimental studies on ABC miktoarms – however, it is possible that some important morphologies may have been missed. 2D phases that could play an important role near the center of the diagram and should be included in future work are the [8.6.4;8.6.6;12.6.4] tiling pattern^{10, 18}, [8.6.4;8.8.4;12.6.4;12.8.4] tiling pattern¹⁷, and core-shell hexagonal cylinders – this last phase is unlikely to be stable near the center but should be considered regardless until it is known for a fact that it does not play a role here. 3D phases that need to be considered in future work include the core-shell variants of the known diblock phases (such as BCC, FCC, gyroid, etc.), the HHC morphology¹⁸, and various others that can be picked from experimental results²¹ and Ref. 12. While the discrepancies between the phase diagram presented in Fig. 3.3b and that in Fig. 1.5 lead us to question the accuracy of their computations,

the enormous number of 3D morphologies they present (that are all solutions of the SCF equations) makes it an excellent reference for choosing candidate morphologies outside the center of the phase diagram.

Despite the progress made thus far on our understanding of miktoarm phase behavior with SCFT there is still much left to be done. With this work, the behavior of the center of the diagram has been established definitively by building on the efforts of past studies – however, the outer region of the phase diagram is still poorly understood, and demands the consideration of more 3D phases beyond the simple morphologies known from diblocks. Further, even the center of the diagram still has some discrepancies that need to be resolved, such as the re-entry of HPL observed in this study. Before extending research to asymmetric interaction parameters, our understanding of the effect of composition should be further refined and the phase diagram mapped out completely for a degree of segregation such as $\chi N = 30$. Once this has been accomplished, the segregation strength should be increased systematically to study its effect on phase behavior and only then the various combinations of asymmetric interactions studied in detail. The results presented in this thesis provide an excellent basis for this future work, and the availability of a high quality open-source software to implement SCFT will hopefully expedite studies on this intriguing class of material.

References

- (1) Frank S. Bates, Glenn H. Fredrickson. Block Copolymers - Designer Soft Materials. *Physics Today* **1999**, 32-38.
- (2) Cheolmin Park, Jongseung Yoon, Edwin L. Thomas. Enabling nanotechnology with self assembled block copolymer patterns. *Polymer* **2003**, 44, 6725-6760.
- (3) Mark W. Matsen, Michael Schick. Stable and Unstable Phases of a Diblock Copolymer Melt. *Physical Review Letters* **1994**, 72, 2660-2663.
- (4) Glenn H. Fredrickson. *The Equilibrium Theory of Inhomogeneous Polymers*; Oxford University Press, 2005.
- (5) Akash Arora, Jian Qin, David C. Morse, Kris T. Delaney, Glenn H. Fredrickson, Frank S. Bates, Kevin D. Dorfman. Broadly Accessible Self-Consistent Field Theory for Block Polymer Materials Discovery. *Macromolecules* **2015**, 49, 4675-4690.
- (6) Frank S. Bates, Marc A. Hillmyer, Timothy P. Lodge, Christopher M. Bates, Kris T. Delaney, Glenn H. Fredrickson. Multiblock Polymers: Panacea or Pandora's Box? *Science* **2012**, 336, 434-440.
- (7) Eugene Helfand. Theory of inhomogeneous polymers: Fundamentals of the Gaussian random-walk model. *Journal of Chemical Physics* **1975**, 62, 999-1005.
- (8) Francois Drolet, Glenn H. Fredrickson. Combinatorial Screening of Complex Block Copolymer Assembly with Self-Consistent Field Theory. *Physical Review Letters* **1999**, 83, 4317-4320.
- (9) Mark W. Matsen. The standard Gaussian model for block copolymer melts. *Journal of Physics: Condensed Matter* **2002**, 14, R21-R27.
- (10) Kenichi Hayashida, Atsushi Takano, Shigeo Arai, Yuya Shinohara, Yoshiyuki Amemiya, Yushu Matsushita. Systematic Transitions of Tiling Patterns Formed by ABC Star-Shaped Terpolymers. *Macromolecules* **2006**, 39, 9402-9408.
- (11) Kazunari Ueda, Tomonari Dotera, Tohru Gemma. Photonic band structure calculations of two-dimensional Archimedean tiling patterns. *Physical Review B* **2007**, 75, 195122.
- (12) Weiquan Xu, Kai Jiang, Pingwen Zhang, An-Chang Shi. A Strategy to Explore Stable and Metastable Ordered Phases of Block Copolymers. *The Journal of Physical Chemistry B* **2013**, 117, 5296-5305.
- (13) Jicheol Park, Sangshin Jang, Jin Kon Kim. Morphology and Microphase Separation of Star Copolymers. *Journal of Polymer Science* **2014**, 53, 1-21.
- (14) G. Tzeremes, K. O. Rasmussen, T. Lookman, A. Saxena. Efficient computation of the structural phase behavior of block copolymers. *Physical Review E* **2002**, 65, 041806.
- (15) Guo Kang Cheong, Anshul Chawla, David C. Morse, Kevin D. Dorfman. Open-source code for self-consistent field theory calculations of block polymer phase behavior on graphics processing units. *The European Physical Journal E* **2020**, 43, 1-8.
- (16) Ping Tang, Feng Qiu, Hongdong Zhang, Yuliang Yang. Morphology and Phase Diagram of Complex Block Copolymers: ABC Star Triblock Copolymers. *The Journal of Physical Chemistry B* **2004**, 108, 8434-8438.
- (17) Guojie Zhang, Feng Qiu, Hongdong Zhang, Yuliang Yang, An-Chang Shi. SCFT Study of Tiling Patterns in ABC Star Terpolymers. *Macromolecules* **2010**, 43, 2981-2989.

- (18) Weihua Li, Yuci Xu, Guojie Zhang, Feng Qiu, Yuliang Yang, An-Chang Shi. Real-space self-consistent mean-field theory study of ABC star triblock copolymers. *The Journal of Chemical Physics* **2010**, *133*, 064904.
- (19) Amit Ranjan, Jian Qin, David C. Morse. Linear Response and Stability of Ordered Phases of Block Copolymer Melts. *Macromolecules* **2008**, *41*, 942-954.
- (20) Kenichi Hayashida, Noriyuki Saito, Shigeo Arai, Atsushi Takano, Nobua Tanaka, Yushu Matsushita. Hierarchical Morphologies Formed by ABC Star-Shaped Terpolymers. *Macromolecules* **2007**, *40*, 3695-3699.
- (21) Yushu Matsushita, Kenichi Hayashida, Tomonari Dotera, Atsushi Takano. Kaleidoscopic morphologies from ABC star-shaped terpolymers. *Journal of Physics: Condensed Matter* **2011**, *23*, 284111.
- (22) Kai Jiang, Juan Zhang, Qin Liang. Self-Assembly of Asymmetrically Interacting ABC Star Triblock Copolymer Melts. *The Journal of Physical Chemistry B* **2015**, *119*, 14551-14562.
- (23) Mark W. Matsen. Field theoretic approach for block polymer melts: SCFT and FTS. *Journal of Chemical Physics* **2020**, *152*, 110901.